Clemens, S.C., Kuhnt, W., LeVay, L.J., and the Expedition 353 Scientists
Proceedings of the International Ocean Discovery Program Volume 353
publications.iodp.org

doi:10.14379/iodp.proc.353.107.2016

Site U1447[1]

S.C. Clemens, W. Kuhnt, L.J. LeVay, P. Anand, T. Ando, M. Bartol, C.T. Bolton, X. Ding, K. Gariboldi, L. Giosan, E.C. Hathorne, Y. Huang, P. Jaiswal, S. Kim, J.B. Kirkpatrick, K. Littler, G. Marino, P. Martinez, D. Naik, A. Peketi, S.C. Phillips, M.M. Robinson, O.E. Romero, N. Sagar, K.B. Taladay, S.N. Taylor, K. Thirumalai, G. Uramoto, Y. Usui, J. Wang, M. Yamamoto, and L. Zhou[2]

Keywords: International Ocean Discovery Program, IODP, Expedition 353, *JOIDES Resolution*, Site U1447, Indian monsoon, monsoon, Bay of Bengal, Andaman Sea, paleoclimate, paleoceanography, Miocene, Pliocene, Pleistocene, Holocene, Ninetyeast Ridge, Indian Ocean, salinity, orbital, millennial, centennial, abrupt climate change

Contents

1 Background and objectives
2 Operations
5 Lithostratigraphy
12 Biostratigraphy
16 Geochemistry
19 Paleomagnetism
24 Physical properties
28 Stratigraphic correlation
30 References

Background and objectives

The Andaman Sea is situated between the Andaman Islands and the Malay Peninsula (Figure **F1**). The Andaman-Sumatra island arc system results from the oblique subduction of the Indo-Australian plate beneath the Eurasian plate (Singh et al., 2013). Stretching and rifting of the overriding plate during the early Miocene (~25 Ma) resulted in two distinct plates (Sunda and Burma) separated by an active spreading center (Curray, 1991, 2005) located in the deepest portion of the Andaman Sea. An accretionary wedge complex scraped off the subducting slab lies west of the spreading center, forming a series of shallower basins associated with back-thrust faulting within the accreted sediments (Figure **F2**). The Andaman Sea drilling sites are within the Nicobar-Andaman Basin, bounded on either side by the Diligent and Eastern margin faults.

Figure F1. Andaman Sea map with location of Site U1447. Map was generated using GeoMapApp (**http://www.geomapapp.org**).

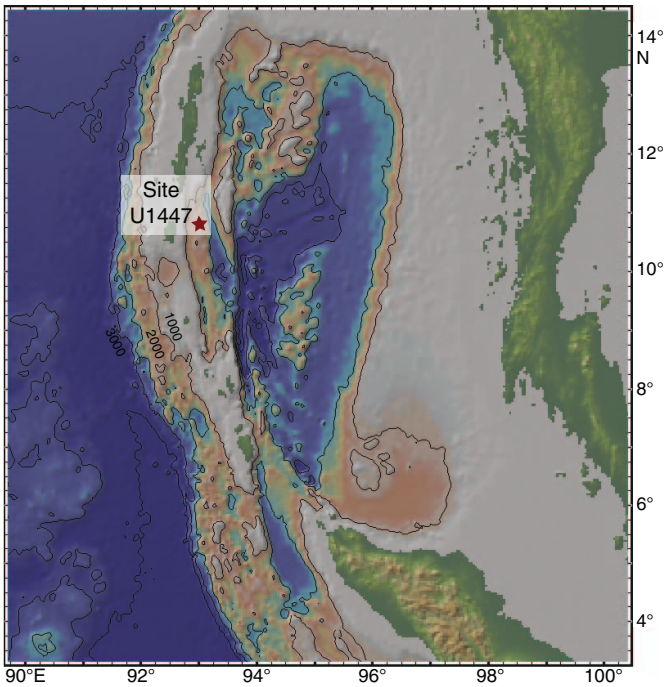

Runoff into the Andaman Sea is dominated by the Irrawaddy and Salween Rivers (Varkey et al., 1996), supplying a combined 30.8 × 10^{10} m^3 of water during June, July, and August. Comparison with the winter (December, January, and February) discharge of 2.8 × 10^{10} m^3, indicates strong seasonality with a dominance of summer (92%) over winter (8%) runoff. Terrigenous sediment supply to the Andaman Sea is dominantly from the Irrawaddy and Salween Rivers (Colin et al., 1999, 2006) with contributions from the Indo-Burman-Arakan mountain ranges as well as the Andaman Islands (Awasthi et al., 2014). However, by virtue of proximity, Little Andaman Island is likely a dominant source of terrigenous materials to International Ocean Discovery Program (IODP) Site U1447. Analysis of Andaman Sea surface sediments indicates that foraminifers are abundant and well preserved shallower than ~1800 meters below sea level (mbsl) (>100,000 individuals/g) and decrease to <100 individuals/g deeper than 3000 mbsl (Frerichs, 1971).

Site U1447 is located at 1391 mbsl, ~45 km offshore Little Andaman Island within a basin on the eastern flank of a rise separating north-south–oriented basins associated with the Eastern Margin and Diligent fault zones. Seismic sections (Figure **F3**) indicate ~740 m of sediments overlying an accretionary wedge complex. Sedimentation rates at Site NGHP-01-17 (Collett et al., 2008; Flores et al., 2014) suggest that the base of this site will be late Miocene in age. A series of hard reflectors from 0.30 to 0.38 s two-way traveltime

[1] Clemens, S.C., Kuhnt, W., LeVay, L.J., Anand, P., Ando, T., Bartol, M., Bolton, C.T., Ding, X., Gariboldi, K., Giosan, L., Hathorne, E.C., Huang, Y., Jaiswal, P., Kim, S., Kirkpatrick, J.B., Littler, K., Marino, G., Martinez, P., Naik, D., Peketi, A., Phillips, S.C., Robinson, M.M., Romero, O.E., Sagar, N., Taladay, K.B., Taylor, S.N., Thirumalai, K., Uramoto, G., Usui, Y., Wang, J., Yamamoto, M., and Zhou, L., 2016. Site U1447. *In* Clemens, S.C., Kuhnt, W., LeVay, L.J., and the Expedition 353 Scientists, *Indian Monsoon Rainfall*. Proceedings of the International Ocean Discovery Program, 353: College Station, TX (International Ocean Discovery Program). http://dx.doi.org/10.14379/iodp.proc.353.107.2016
[2] **Expedition 353 Scientists' addresses.**
MS 353-107: Published 29 July 2016

Figure F2. Summary sketch after Singh et al. (2013) showing the subduction zone through the back-arc basin to ~40 km depth. DF = Diligent fault, NAB = Nicobar-Andaman Basin, ANF = Andaman-Nicobar fault.

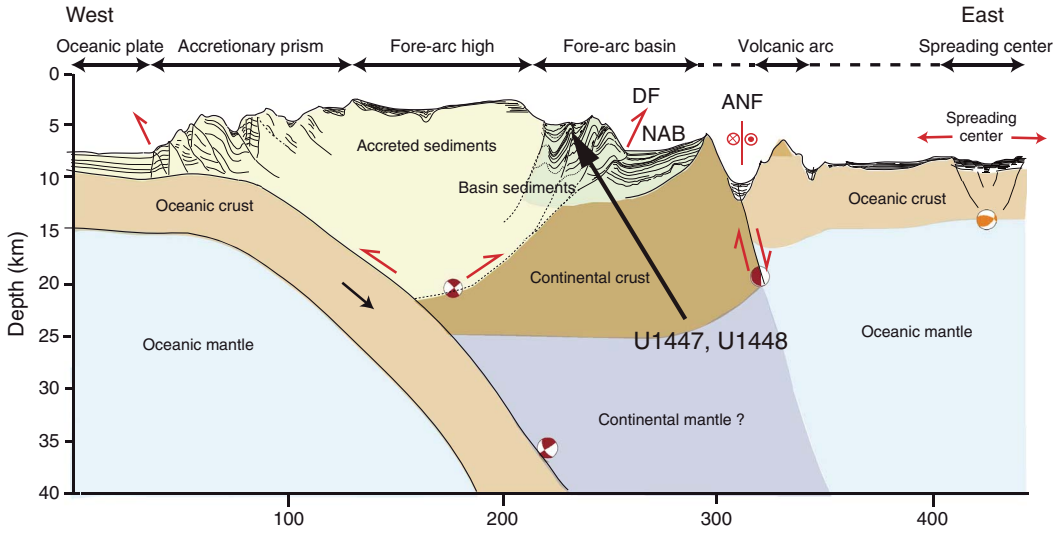

Figure F3. Seismic lines showing location of Site U1447.

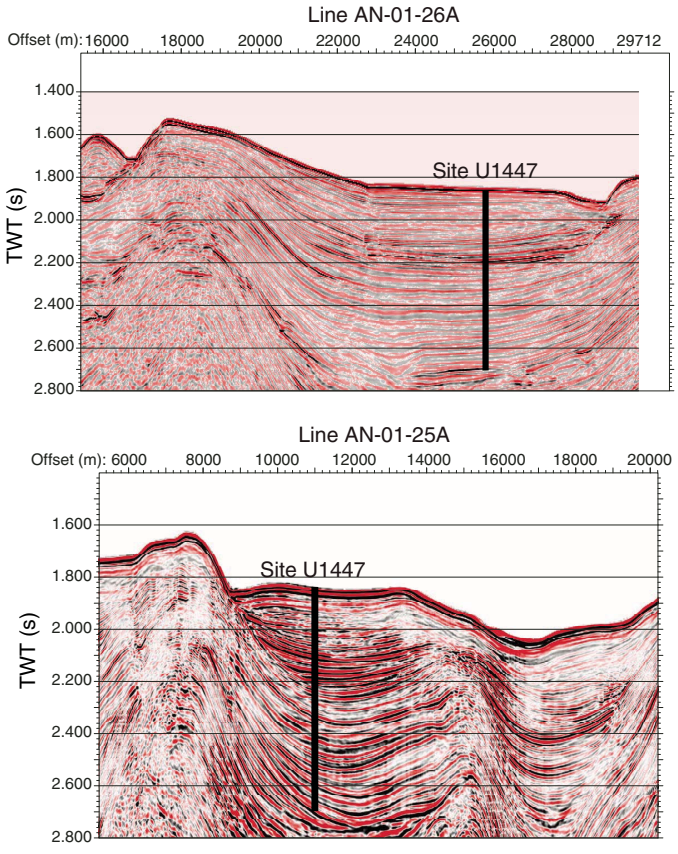

(TWT) below the seafloor is interpreted as an interval of coarse sediments.

The objective at this site is to recover Miocene to Holocene sediments from multiple holes in order to reconstruct changes in surface water salinity and runoff associated with summer monsoon rainfall at tectonic to suborbital timescales. Sites U1448 and U1447 will constitute the middle (10°N) portion of a meridional salinity transect that includes sites on the northeast Indian margin (19°N) and is anchored by IODP Site U1443 at 5°N.

Operations

Site U1447 consisted of three holes (Table **T1**), ranging in depth from 24.4 to 738.0 m drilling depth below seafloor (DSF). Overall, 108 cores were recorded for the site. A total of 451.27 m of core over a 444.3 m cored interval was recovered using the advanced piston corer (APC) system (102% recovery). The cored interval with the half-length advanced piston corer (HLAPC) system was 67.8 m with a core recovery of 69.12 m (102%). The cored interval with the extended core barrel (XCB) system was 409.2 m with 395.15 m of core recovered (97%). The overall recovery percentage for Site U1447 was 99%. The total time spent on Site U1447 was 6.1 days.

Transit to Site U1447

After a 709 nmi transit from Site U1446, the vessel arrived at Site U1447. The thrusters were lowered and dynamic positioning assumed control at 1430 h (UTC + 8 h) on 15 January 2015.

Hole U1447A

Hole U1447A was spudded at 2320 h on 15 January 2015. Core 353-U1447A-1H was used to estimate the seafloor depth at 1390.9 mbsl. The APC system was used for Cores 1H through 29H. The HLAPC was deployed for Cores 30F through 44F. Cores 45X through 88X were cut with the XCB system. Downhole temperature measurements using the third-generation advanced piston corer temperature tool (APCT-3) shoe were taken on Cores 4H, 7H, 10H, and 15H. The Icefield MI-5 tool was used to obtain orientation data for Cores 3H through 29H. After coring operations, the hole was displaced with heavy mud and the pipe was pulled from the hole. The pipe cleared the seafloor at 1705 h on 20 January.

A total of 29 APC cores were taken over a 261.0 m interval with a total core recovery of 268.69 m (103% core recovery). The HLAPC system was used for 15 cores over a cored interval of 67.8 m with 69.12 m recovered (102%). A total of 44 XCB cores were cut over a

Table T1. Site U1447 core summary. CSF = core depth below seafloor, DRF = drilling depth below rig floor, DSF = drilling depth below seafloor, mbsl = meters below sea level. F = half-length advanced piston corer, H = advanced piston corer, X = extended core barrel, numeric core type = drilled interval. (Continued on next two pages.) **Download table in .csv format.**

Hole U1447A
Latitude: 10°47.4061′N
Longitude: 92°59.9999′E
Time on hole (h): 122.5
Seafloor (drill pipe measurement below rig floor, m DRF): 1402.2
Distance between rig floor and sea level (m): 11.3
Water depth (drill pipe measurement from sea level, mbsl): 1390.9
Total penetration (drilling depth below seafloor, m DSF): 2140.2
Total length of cored section (m): 738
Total core recovered (m): 732.96
Core recovery (%): 99
Total number of cores: 88

Hole U1447B
Latitude: 10°47.3945′N
Longitude: 93°00.0028′E
Time on hole (h): 5.25
Seafloor (drill pipe measurement below rig floor, m DRF): 1403.1
Distance between rig floor and sea level (m): 11.3
Water depth (drill pipe measurement from sea level, mbsl): 1391.8
Total penetration (drilling depth below seafloor, m DSF): 1427.5
Total length of cored section (m): 24.4
Total core recovered (m): 24.26
Core recovery (%): 99
Total number of cores: 3

Hole U1447C
Latitude: 10°47.3952′N
Longitude: 93°00.0114′E
Time on hole (h): 19.25
Seafloor (drill pipe measurement below rig floor, m DRF): 1403.6
Distance between rig floor and sea level (m): 11.3
Water depth (drill pipe measurement from sea level, mbsl): 1392.3
Total penetration (drilling depth below seafloor, m DSF): 1564.5
Total length of cored section (m): 158.9
Total core recovered (m): 158.32
Core recovery (%): 100
Total number of cores: 17

			Depth DSF (m)			Depth CSF (m)				
Core	Date (2015)	Time UTC (h)	Top of cored interval	Bottom of cored interval	Interval advanced (m)	Top of cored interval	Bottom of cored interval	Length of core recovered (m)	Recovery (%)	Sections (*N*)
353-U1447A-										
1H	15 Jan	1530	0.0	3.3	3.3	0.0	3.37	3.37	102	4
2H	15 Jan	1620	3.3	12.8	9.5	3.3	12.72	9.42	99	8
3H	15 Jan	1705	12.8	22.3	9.5	12.8	22.73	9.93	105	8
4H	15 Jan	1750	22.3	31.8	9.5	22.3	32.28	9.98	105	8
5H	15 Jan	1835	31.8	41.3	9.5	31.8	41.67	9.87	104	8
6H	15 Jan	1910	41.3	50.8	9.5	41.3	51.27	9.97	105	8
7H	15 Jan	2000	50.8	60.3	9.5	50.8	60.66	9.86	104	8
8H	15 Jan	2045	60.3	69.8	9.5	60.3	70.13	9.83	103	8
9H	15 Jan	2130	69.8	79.3	9.5	69.8	79.54	9.74	103	8
10H	15 Jan	2225	79.3	88.8	9.5	79.3	89.48	10.18	107	8
11H	15 Jan	2310	88.8	98.3	9.5	88.8	98.80	10.00	105	8
12H	15 Jan	2350	98.3	107.8	9.5	98.3	107.97	9.67	102	8
13H	16 Jan	0055	107.8	116.5	8.7	107.8	116.50	8.70	100	8
14H	16 Jan	0200	116.5	126.0	9.5	116.5	126.66	10.16	107	8
15H	16 Jan	0255	126.0	135.5	9.5	126.0	136.05	10.05	106	8
16H	16 Jan	0340	135.5	145.0	9.5	135.5	145.57	10.07	106	8
17H	16 Jan	0415	145.0	154.5	9.5	145.0	154.87	9.87	104	8
18H	16 Jan	0450	154.5	164.0	9.5	154.5	164.56	10.06	106	9
19H	16 Jan	0525	164.0	173.5	9.5	164.0	173.90	9.90	104	8
20H	16 Jan	0605	173.5	183.0	9.5	173.5	183.55	10.05	106	9
21H	16 Jan	0635	183.0	192.5	9.5	183.0	192.40	9.40	99	9
22H	16 Jan	0710	192.5	202.0	9.5	192.5	202.71	10.21	107	8
23H	16 Jan	0750	202.0	211.5	9.5	202.0	211.90	9.90	104	9
24H	16 Jan	0825	211.5	221.0	9.5	211.5	221.24	9.74	103	8
25H	16 Jan	0900	221.0	230.5	9.5	221.0	230.68	9.68	102	8
26H	16 Jan	0940	230.5	240.0	9.5	230.5	240.10	9.60	101	8
27H	16 Jan	1015	240.0	249.5	9.5	240.0	248.04	8.04	85	7
28H	16 Jan	1055	249.5	254.9	5.4	249.5	254.88	5.38	100	6
29H	16 Jan	1140	254.9	261.0	6.1	254.9	260.98	6.08	100	6
30F	16 Jan	1320	261.0	265.8	4.8	261.0	266.01	5.01	104	5
31F	16 Jan	1405	265.8	270.6	4.8	265.8	267.32	1.52	32	2
32F	16 Jan	1435	270.6	275.4	4.8	270.6	275.89	5.29	110	5
33F	16 Jan	1505	275.4	280.2	4.8	275.4	280.73	5.33	111	5
34F	16 Jan	1535	280.2	285.0	4.8	280.2	285.38	5.18	108	6
35F	16 Jan	1610	285.0	289.8	4.8	285.0	290.26	5.26	110	5
36F	16 Jan	1645	289.8	294.6	4.8	289.8	295.03	5.23	109	5
37F	16 Jan	1720	294.6	299.4	4.8	294.6	299.80	5.20	108	5
38F	16 Jan	1810	299.4	304.2	4.8	299.4	304.68	5.28	110	5
39F	16 Jan	1850	304.2	309.0	4.8	304.2	309.44	5.24	109	5

Table T1 (continued). (Continued on next page.)

Core	Date (2015)	Time UTC (h)	Depth DSF (m) Top of cored interval	Depth DSF (m) Bottom of cored interval	Interval advanced (m)	Depth CSF (m) Top of cored interval	Depth CSF (m) Bottom of cored interval	Length of core recovered (m)	Recovery (%)	Sections (*N*)
40F	16 Jan	1930	309.0	313.8	4.8	309.0	314.17	5.17	108	5
41F	16 Jan	2005	313.8	315.0	1.2	313.8	315.01	1.21	101	2
42F	16 Jan	2205	315.0	319.8	4.8	315.0	319.67	4.67	97	5
43F	16 Jan	2315	319.8	324.6	4.8	319.8	325.05	5.25	109	5
44F	17 Jan	0015	324.6	328.8	4.2	324.6	328.88	4.28	102	5
45X	17 Jan	0345	328.8	333.1	4.3	328.8	333.10	4.30	100	4
46X	17 Jan	0455	333.1	342.8	9.7	333.1	333.10	0.00	0	0
47X	17 Jan	0605	342.8	352.5	9.7	342.8	352.89	10.09	104	8
48X	17 Jan	0715	352.5	362.2	9.7	352.5	362.22	9.72	100	8
49X	17 Jan	0835	362.2	371.9	9.7	362.2	372.09	9.89	102	8
50X	17 Jan	0945	371.9	381.6	9.7	371.9	381.12	9.22	95	8
51X	17 Jan	1110	381.6	391.3	9.7	381.6	391.35	9.75	101	8
52X	17 Jan	1230	391.3	401.0	9.7	391.3	401.26	9.96	103	9
53X	17 Jan	1355	401.0	410.7	9.7	401.0	410.85	9.85	102	8
54X	17 Jan	1520	410.7	420.4	9.7	410.7	420.46	9.76	101	8
55X	17 Jan	1705	420.4	430.1	9.7	420.4	430.04	9.64	99	8
56X	17 Jan	1905	430.1	439.8	9.7	430.1	439.02	8.92	92	7
57X	17 Jan	2110	439.8	449.5	9.7	439.8	449.50	9.70	100	8
58X	17 Jan	2255	449.5	459.2	9.7	449.5	458.31	8.81	91	7
59X	18 Jan	0045	459.2	468.9	9.7	459.2	468.91	9.71	100	8
60X	18 Jan	0220	468.9	478.6	9.7	468.9	478.53	9.63	99	8
61X	18 Jan	0355	478.6	488.3	9.7	478.6	488.06	9.46	98	8
62X	18 Jan	0540	488.3	498.0	9.7	488.3	498.19	9.89	102	8
63X	18 Jan	0725	498.0	507.7	9.7	498.0	507.74	9.74	100	8
64X	18 Jan	0855	507.7	517.4	9.7	507.7	517.49	9.79	101	8
65X	18 Jan	1045	517.4	527.1	9.7	517.4	526.31	8.91	92	7
66X	18 Jan	1240	527.1	536.8	9.7	527.1	537.11	10.01	103	9
67X	18 Jan	1420	536.8	546.5	9.7	536.8	546.39	9.59	99	8
68X	18 Jan	1610	546.5	556.2	9.7	546.5	556.49	9.99	103	9
69X	18 Jan	1805	556.2	565.9	9.7	556.2	566.07	9.87	102	8
70X	18 Jan	1940	565.9	575.6	9.7	565.9	565.90	0.00	0	0
71X	18 Jan	2130	575.6	585.3	9.7	575.6	585.33	9.73	100	9
72X	18 Jan	2320	585.3	595.0	9.7	585.3	594.95	9.65	99	8
73X	19 Jan	0105	595.0	604.7	9.7	595.0	604.87	9.87	102	8
74X	19 Jan	0250	604.7	614.4	9.7	604.7	614.89	10.19	105	8
75X	19 Jan	0435	614.4	624.1	9.7	614.4	624.20	9.80	101	8
76X	19 Jan	0605	624.1	633.8	9.7	624.1	633.80	9.70	100	8
77X	19 Jan	0750	633.8	643.5	9.7	633.8	643.47	9.67	100	9
78X	19 Jan	0935	643.5	647.7	4.2	643.5	651.59	8.09	193	7
79X	19 Jan	1100	647.7	653.3	5.6	647.7	653.92	6.22	111	5
80X	19 Jan	1255	653.3	663.0	9.7	653.3	663.31	10.01	103	8
81X	19 Jan	1525	663.0	672.7	9.7	663.0	672.56	9.56	99	8
82X	19 Jan	1755	672.7	682.4	9.7	672.7	682.49	9.79	101	9
83X	19 Jan	2010	682.4	692.1	9.7	682.4	692.17	9.77	101	8
84X	19 Jan	2150	692.1	701.8	9.7	692.1	700.10	8.00	82	7
85X	20 Jan	0005	701.8	711.5	9.7	701.8	711.45	9.65	99	8
86X	20 Jan	0135	711.5	721.2	9.7	711.5	721.39	9.89	102	9
87X	20 Jan	0300	721.2	730.9	9.7	721.2	731.00	9.80	101	8
88X	20 Jan	0435	730.9	738.0	7.1	730.9	740.46	9.56	135	8
353-U1447B-										
1H	20 Jan	1300	0.0	5.4	5.4	0.0	5.47	5.47	101	5
2H	20 Jan	1340	5.4	14.9	9.5	5.4	14.64	9.24	97	8
3H	20 Jan	1410	14.9	24.4	9.5	14.9	24.45	9.55	101	8
353-U1447C-										
1H	20 Jan	1515	0.0	6.9	6.9	0.0	6.95	6.95	101	6
2H	20 Jan	1555	6.9	16.4	9.5	6.9	15.22	8.32	88	7
31	20 Jan	1615				*****Drilled interval 16.4–18.4 m DSF*****				
4H	20 Jan	1635	18.4	27.9	9.5	18.4	27.82	9.42	99	8
5H	20 Jan	1705	27.9	37.4	9.5	27.9	37.79	9.89	104	8
6H	20 Jan	1755	37.4	46.9	9.5	37.4	47.27	9.87	104	8
7H	20 Jan	1820	46.9	56.4	9.5	46.9	56.81	9.91	104	8
8H	20 Jan	1855	56.4	65.9	9.5	56.4	66.27	9.87	104	8
9H	20 Jan	1925	65.9	75.4	9.5	65.9	75.74	9.84	104	8
10H	20 Jan	2000	75.4	84.9	9.5	75.4	84.73	9.33	98	8
11H	20 Jan	2035	84.9	94.4	9.5	84.9	94.89	9.99	105	8
12H	20 Jan	2110	94.4	103.9	9.5	94.4	103.30	8.90	94	7
13H	20 Jan	2155	103.9	113.4	9.5	103.9	114.15	10.25	108	8

Table T1 (continued).

Core	Date (2015)	Time UTC (h)	Depth DSF (m) Top of cored interval	Depth DSF (m) Bottom of cored interval	Interval advanced (m)	Depth CSF (m) Top of cored interval	Depth CSF (m) Bottom of cored interval	Length of core recovered (m)	Recovery (%)	Sections (*N*)
14H	20 Jan	2235	113.4	122.9	9.5	113.4	123.21	9.81	103	9
15H	21 Jan	0005	122.9	132.4	9.5	122.9	133.45	10.55	111	8
16H	21 Jan	0150	132.4	141.9	9.5	132.4	137.55	5.15	54	5
17H	21 Jan	0310	141.9	151.4	9.5	141.9	151.92	10.02	105	9
18H	21 Jan	0345	151.4	160.9	9.5	151.4	161.65	10.25	108	9

409.2 m interval with 395.15 m of core recovered (97%). Total core recovery for Hole U1447A was 99%.

Hole U1447B

The vessel was offset 20 m south of Hole U1447A, and Hole U1447B was spudded at 2045 h on 20 January 2015. Cores 353-U1447B-1H through 3H were recovered and sampled for high-resolution pore water chemistry. The pipe was pulled from the hole and cleared the seafloor at 2220 h.

A total of three APC cores were taken over a 24.4 m interval with a total core recovery of 24.26 m (99% core recovery).

Hole U1447C

The vessel was offset 20 m east of Hole U1447B, and Hole U1447C was spudded at 2300 h on 20 January 2015. Cores 353-U1447C-1H through 18H were cored with the APC system to a total depth of 160.9 m. A 2 m drilled interval (353-U1447C-31) extended from 16.4 to 18.4 m DSF. Cores 4H through 16H were oriented using the Icefield MI-5 tool. At the end of coring operations, the pipe was pulled from the hole and cleared the seafloor at 1405 h on 21 January. The remaining drill pipe was tripped during the 9.4 nmi transit to Site U1448.

A total of 17 APC cores were taken over a 158.9 m cored interval with a total core recovery of 158.32 m (100% core recovery).

Lithostratigraphy

Sediments recovered from Holes U1447A–U1447C are principally composed of Late Pleistocene to late Miocene hemipelagic clays with a significant biogenic component, as well as a large number of calcitic turbidites, of Late Pleistocene to late Miocene age, comprising four distinct lithostratigraphic units (I–IV) (Figure **F4**). Unit I is 126 m thick and comprised of Late Pleistocene greenish gray clayey nannofossil ooze with foraminifers and foraminifer-rich nannofossil ooze with clay. Unit II is 193 m thick, comprised of Late Pleistocene to late Pliocene greenish gray clayey nannofossil ooze with foraminifers, foraminifer-rich nannofossil ooze with clay, and clayey calcareous ooze with varying proportions of foraminifers. This unit is also characterized by the presence of numerous thin to thick light gray beds of foraminifer-rich or bioclastic carbonate fragments of sand–silt size, interpreted as turbidites because of the presence of normal grading and coarser grain size compared to the surrounding hemipelagic sediment. Unit III is 180 m thick, comprised of early Pliocene to late Miocene greenish gray clayey nannofossil ooze to calcareous ooze with varying amounts of glauconite. Unit IV is composed of late Miocene greenish gray–gray clayey nannofossil ooze with glauconite or biosilica, biosilica-rich clay with varying proportions of glauconite and nannofossils, and nannofossil-rich clay with biosilica. The observed lithologic differences between units are principally the result of variations in biosilica abundance (predominantly diatoms and sponge spicules), turbidites, and nannofossils (Figure **F5**). Lithologic descriptions are based primarily on sediments recovered from Hole U1447A, supplemented with observations from Hole U1447C.

Unit I

Intervals: 353-U1447A-1H-1, 0 cm, through 14H-CC, 3 cm;
353-U1447B-1H-1, 0 cm, through 3H-CC, 15 cm;
353-U1447C-1H-1, 0 cm, through 15H-CC, 30 cm
Depths: Hole U1447A = 0–126.00 m core depth below seafloor, Method A (CSF-A);
Hole U1447B = 0–24.45 m CSF-A;
Hole U1447C = 0–133.54 m CSF-A
Age: Late Pleistocene
Major lithology: clayey nannofossil ooze with foraminifers and foraminifer-rich nannofossil ooze with clay
Minor lithology: volcanic ash and foraminifer-rich and/or bioclastic sand/silt

Unit I is a ~126 m thick succession of light greenish gray (GLEY 1 5/10Y) clayey nannofossil ooze with foraminifers and foraminifer-rich nannofossil ooze with clay (Figures **F4**, **F6**, **F7**). Calcareous nannofossils make up ~30%–50% in smear slide samples, followed by foraminifers (10%–30%), clay (10%–40%), and biosilica, which is dominated by sponge spicules and diatoms (~10%) (Figure **F8**). Physical property data is relatively invariant within Unit I, although there is a minor decrease in b* downhole (see **Physical properties**). Two thick (93.5 and 20 cm) turbidites composed of sand and bioclastic sand, respectively, are present in sediments from Unit I (intervals 353-U1447A-2H-1, 0–93.5 cm, and 9H-6, 7–29 cm) (Figure **F9**). Two light gray vitric ash layers (6 and 63 cm thick) are also present in Unit I (intervals 3H-3, 21–27 cm, and 12H-5, 42–105 cm). A bioclastic sand from interval 353-U1447B-1H-4, 38 cm, also contains lithic fragments, including a fragment of serpentinite (Figure **F10**). A 5.5 cm thick light gray ash at 16.21–16.26 m CSF-A (interval 353-U1447B-3H-1, 130.5–136 cm) is tentatively identified as the Late Pleistocene Toba ash event but was not observed in Holes U1447A or U1447C. Drilling disturbance is minor with only occasional horizontal cracks.

Unit II

Intervals: 353-U1447A-14H-CC, 3 cm, through 45F-1, 32 cm;
353-U1447C-15H-CC, 30 cm, through 18H-CC, 22 cm
Depths: Hole U1447A = 126.00–329.12 m CSF-A;
Hole U1447C = 133.54–162 m CSF-A
Age: Late Pleistocene to late Pliocene

Figure F4. Lithostratigraphic summary, Site U1447. All unit divisions are plotted relative to Hole U1447A. Details of each core are available in the visual core description logs.

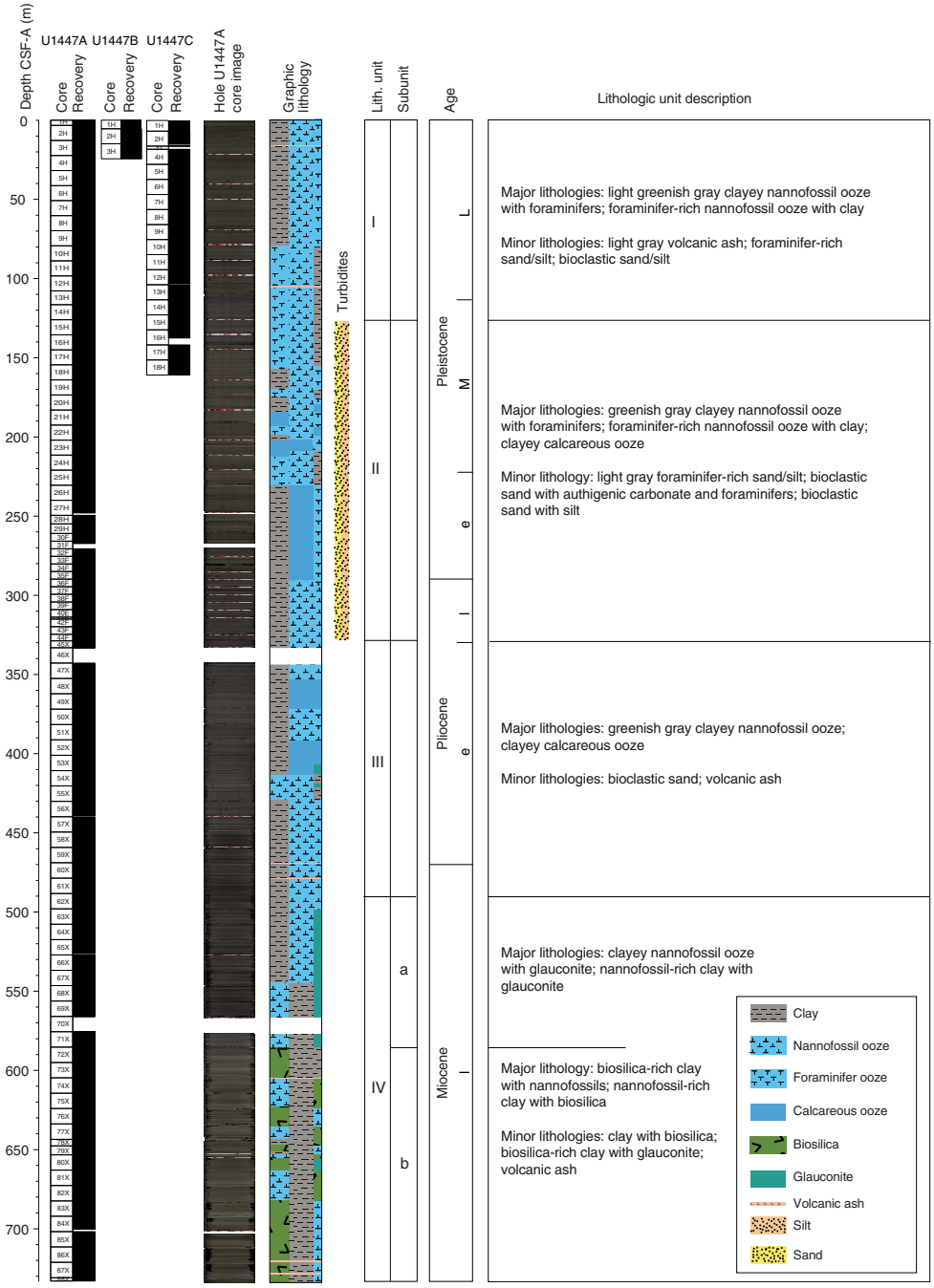

Major lithology: Clayey nannofossil ooze with foraminifers, foraminifer-rich nannofossil ooze with clay, and clayey calcareous ooze

Minor lithology: foraminifer-rich sand/silt and bioclastic sand with authigenic carbonate and foraminifers

Unit II is a ~193 m thick succession of greenish gray (GLEY 1 4/10Y to GLEY 1 5/10Y) clayey nannofossil ooze with foraminifers, foraminifer-rich nannofossil ooze with clay, and clayey calcareous ooze with varying proportions of foraminifers (Figures **F4**, **F6**, **F7**). Between 170 and 300 m CSF-A, the proportion and preservation of calcareous nannofossils and foraminifers decreases and the proportion of authigenic carbonate increases (Figure **F8**). The biosiliceous component within Unit II is predominantly composed of sponge spicules with virtually no contribution from other biosiliceous organisms. There is a minor downhole decrease in b* and L* and an increase in natural gamma radiation (NGR) and magnetic susceptibility (MS) within Unit II (see **Physical properties**). Numerous light gray (2.5Y 7/2) calcitic turbidites are observed in Unit II, composed of foraminifer-rich sand to clay and bioclastic sand with authigenic carbonate and foraminifers, varying in thickness from 1 to 80 cm (Figures **F9**, **F11**). The frequency of turbidites and the percentage of each core composed of turbidites increases downhole, peaks be-

Figure F5. Lithostratigraphic summary with selected physical property and geochemical data from Holes U1447A–U1447C plotted against depth. MS = magnetic susceptibility, NGR = natural gamma radiation.

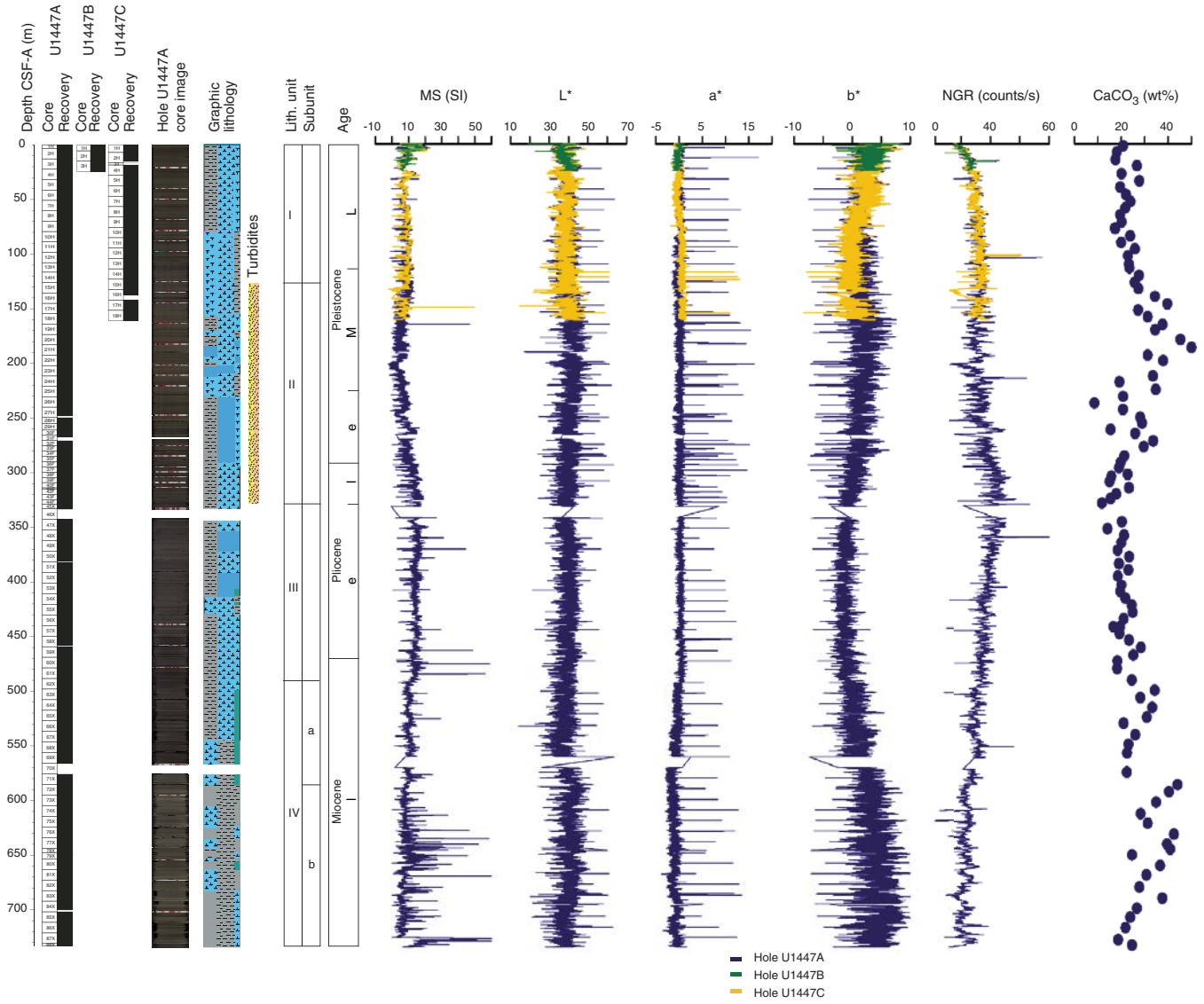

tween 160 and 220 m CSF-A, and then decreases downhole until the last turbidite is observed at 329.12 m CSF-A (interval 353-U1447A-45X-1, 29–32 cm), marking the base of the unit (Figure **F11**). Variations in the frequency and number of turbidites per meter is inversely correlated with nannofossil and clay abundance, whereas authigenic carbonate content positively correlates with turbidite frequency (Figures **F8**, **F11**). Smear slide observations demonstrate that Unit II turbidites between 130 and 144 m CSF-A are dominated by foraminifers (Figures **F8**, **F11**), whereas calcareous bioclasts are the dominant component deeper than 144 m CSF-A, with quartz content increasing between 260 and 297 m CSF-A (Figure **F11**). Comparison of X-ray diffraction (XRD) data from the bioclastic turbidites and surrounding nannofossil ooze shows an increase in aragonite and high-Mg calcite within the calcitic turbidites (Figure **F10**). Drilling disturbance is minor with only occasional horizontal cracks observed.

Unit III

Interval: 353-U1447A-45F-1, 32 cm, through 62X-2, 0 cm
Depth: Hole U1447A = 329.12–489.80 m CSF-A
Age: late Pliocene to late Miocene
Major lithology: clayey nannofossil ooze and clayey calcareous ooze
Minor lithology: clayey nannofossil ooze with foraminifers, clayey calcareous ooze with glauconite, nannofossil ooze with clay, and volcanic ash

Unit III is a ~182 m thick succession of greenish gray (GLEY 1 5/5GY to GLEY 1 5/10GY) clayey nannofossil ooze or clayey calcareous ooze with varying glauconite abundance, further characterized by a complete absence of biosiliceous components (Figures **F6**, **F7**, **F8**). Within the clayey nannofossil ooze, faint color variations from dark gray (GLEY 1 3/5GY) to lighter gray (GLEY 1 5/5GY), or more

Figure F6. Line scan images of main lithologies, Site U1447. A. Clayey nannofossil ooze with foraminifers, Unit I. B. Foraminifer-rich nannofossil ooze with clay, Unit II. C. Clayey nannofossil ooze with glauconite, Unit III. D. Clayey nannofossil ooze with glauconite, with minor drilling disturbance, Subunit IVa. E. Biosilica-rich clay with nannofossils, Subunit IVb.

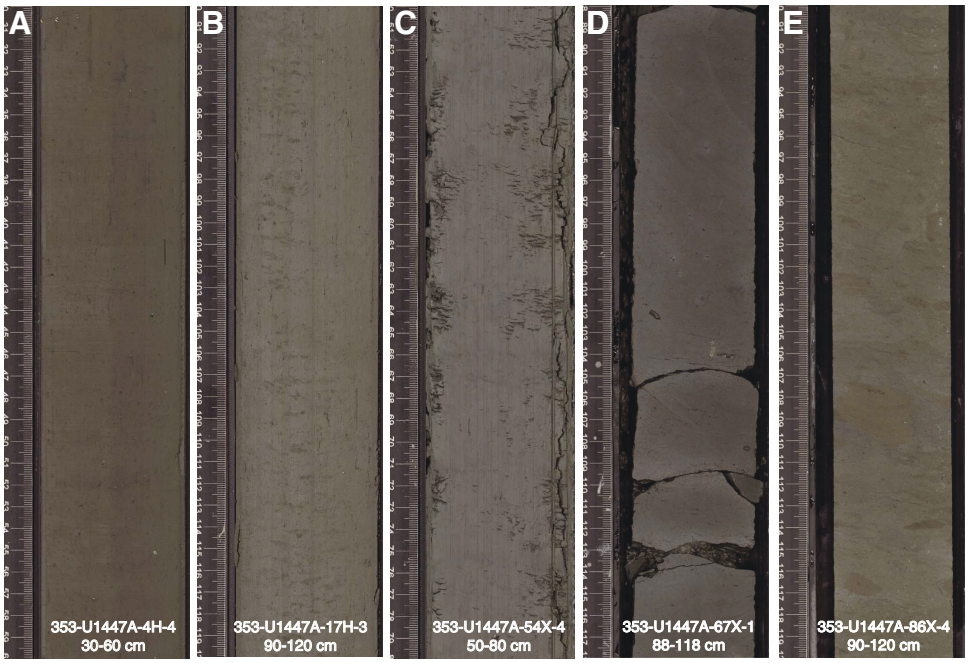

Figure F7. Photomicrographs of the main lithologies, Site U1447. A. Foraminifer-rich nannofossil ooze with clay, Unit I. B. Authigenic carbonate-rich nannofossil ooze with foraminifers, Unit II. C. Clay with nannofossils, Unit III. D. Biosilica-rich clay with nannofossils, Unit IV. E. Volcanic ash, Unit I. F. Bioclastic sand, Unit II. PPL = plane-polarized light, XPL = cross-polarized light.

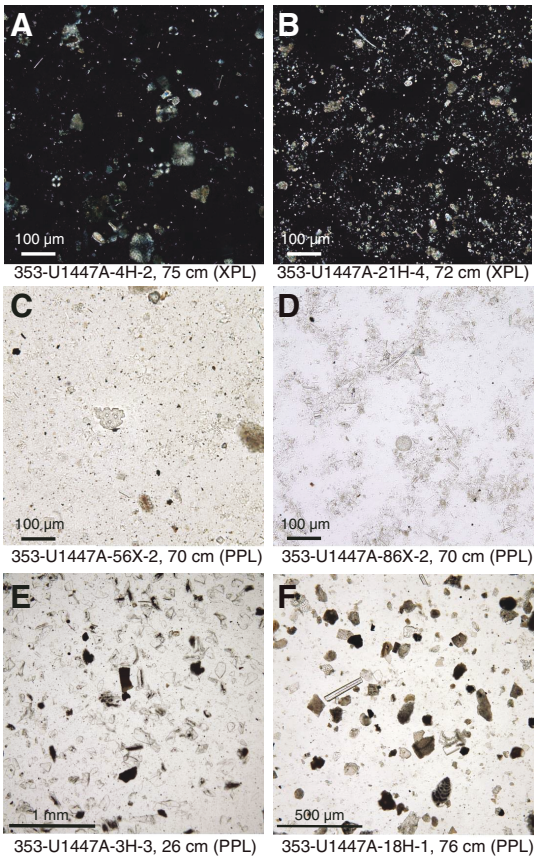

brownish gray (GLEY 1 5/10Y), are common. The composition of the different colored oozes is very similar, except for slightly higher foraminifer content in the brownish gray intervals. Deeper than 425 m CSF-A, calcareous nannofossil content increases up to 60% with a corresponding decrease in the proportion of clays, reflected in a downhole decrease in NGR (Figure **F5**; see **Physical properties**). Authigenic carbonate is more common near the top of the unit (~350–425 m CSF-A) and decreases in abundance downhole. A key characteristic of Unit III is the absence of any biosiliceous components, including the sponge spicules that were ubiquitous in Units I and II (Figure **F8**); indeed, the base of Unit III is defined by the occurrence of the first sponge spicule-bearing interval in Section 353-U1447A-62X-2. Rare volcanic ashes are preserved as pale blebs (interval 53X-6, 3–8 cm) or thin dark gray beds (interval 54X-1, 7–12 cm) (Figure **F9**). No turbidites were observed in Unit III. Drilling disturbance is slight to moderate, with frequent biscuiting, coincident with the change to XCB coring at the top of the unit.

Unit IV

Interval: 353-U1447A-62X-2, 0 cm, through 88X-CC, 83 cm
Depth: Hole U1447A = 489.80–740.46 m CSF-A
Age: late Miocene
Major lithology: clayey nannofossil ooze with glauconite, biosilica-rich clay with nannofossils, and nannofossil-rich clay with biosilica
Minor lithology: volcanic ash

Unit IV is a ~182 m thick succession of greenish gray (GLEY 1 5/5GY to GLEY 1 5/10GY) clayey nannofossil ooze with glauconite, biosilica-rich clay with nannofossils, and nannofossil-rich clay with biosilica (Figures **F6**, **F7**, **F8**). Unit IV is considerably richer in biosilica than Units I–III, with biosiliceous content increasing with depth, reflecting an increase in both the proportion of sponge spicules and diatoms (Figure **F8**). Foraminifers are a more minor com-

Figure F8. Smear slide data, Holes U1447A and U1447C.

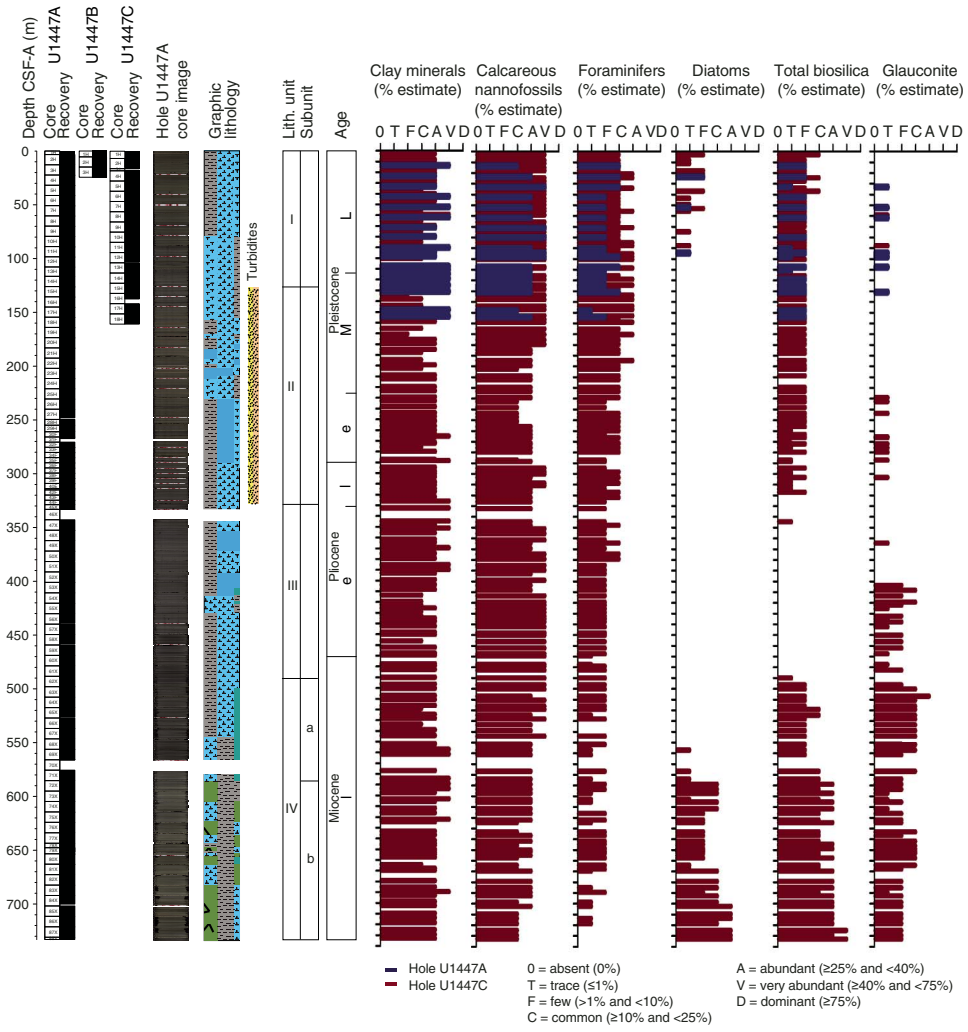

ponent of the sediment relative to Units I–III. Unit IV is divided into two subunits: Subunit IVb is distinguished from IVa by a substantial increase in biosilica downhole, particularly diatoms, which reach a maximum at the base of the hole between Cores 353-U1447A-84X and 88X. The b* values increase strongly downhole, peaking in Subunit IVb, whereas NGR values steadily decrease as the amount of biosilica increases (Figure **F5**). MS values peak in Subunit IVb between 630 and 670 m CSF-A. One volcanic ash was noted at interval 74X-1, 11–17 cm. No turbidites were observed in Unit IV. Drilling disturbance in this unit is slight to severe, most commonly present as biscuiting (Figure **F6**).

Subunit IVa

Interval: 353-U1447A-62X-2, 0 cm, through 71X-CC, 25 cm
Depth: Hole U1447A = 489.80–585.33 m CSF-A
Age: late Miocene
Major lithology: clayey nannofossil ooze with glauconite and nannofossil-rich clay with glauconite

Subunit IVa is a ~77 m thick succession of greenish gray (GLEY 1 5/5GY to GLEY 1 5/10Y) clayey nannofossil ooze with glauconite. There are subtle color variations from brownish gray (GLEY 1 5/10Y) to greenish gray (GLEY 1 5/10GY) throughout Subunit IVa. Sponge spicules are present (~7%), and diatoms are rare, whereas the proportions of clays and nannofossils are similar to one another throughout (30%–40%) (Figure **F8**). The first diatoms outside of the Late Pleistocene appear downhole at the base of Subunit IVa. Drilling disturbance in Subunit IVa is slight to severe, most commonly present as biscuiting and with some cracks (Figure **F6**).

Subunit IVb

Interval: 353-U1447A-72X-1, 0 cm, through 88X-CC, 83 cm
Depth: Hole U1447A = 585.33–740.46 m CSF-A
Age: late Miocene
Major lithology: biosilica-rich clay with nannofossils and nannofossil-rich clay with biosilica
Minor lithology: clay with biosilica, biosilica-rich clay with glauconite, and volcanic ash

Subunit IVb is a ~155 m thick succession of greenish gray (GLEY 1 6/5GY to GLEY 1 6/10Y and GLEY 1 4/10Y to GLEY 1 6/10Y) biosilica-rich clay with nannofossils. Biosilica content increases downhole, dominated by diatoms and sponge spicules and matched by a concurrent increase in b* and decrease in NGR (Figures **F5**, **F8**) (see **Physical properties**). There are faint color variations from brownish (GLEY 1 6/10Y) to greenish (GLEY 1 6/10GY)

Figure F9. Line scan images of minor lithologies, Site U1447. A. Volcanic ash likely associated with the Late Pleistocene Toba eruption, Unit I. B. Gray volcanic ash with clay, Unit I. C. Light gray bleb of volcanic ash with glauconite, Unit III. D. Very dark gray volcanic ash, Unit III. E. Thick turbidite with coarse sand, shell fragments, and foraminifers, Unit I. F. Bioclastic sandy blebs and thin bioclastic turbidite layers, Unit II. G. Dark patches of plant debris, Unit I.

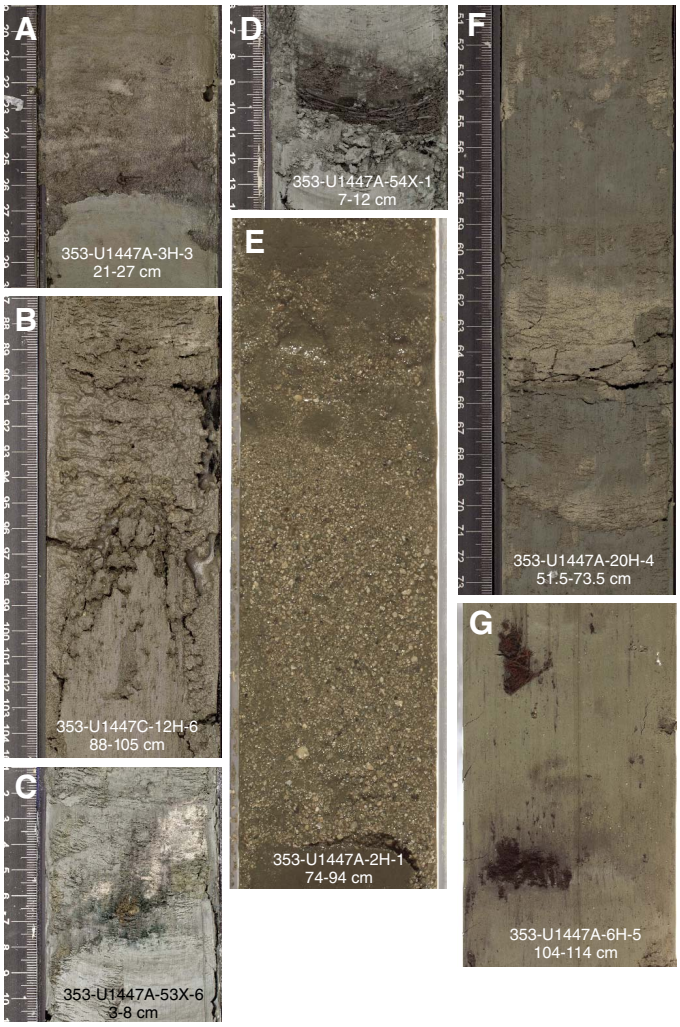

gray, and from lighter (GLEY 1 7/5GY) to dark greenish gray (GLEY 1 5/5GY), throughout. Brown patches with more abundant foraminifers and green patches with more abundant glauconite are common throughout Subunit IVb (Figure F8). Heavy bioturbation is visible throughout Subunit IVb in the form of mottling and burrows of various sizes and morphologies. Drilling disturbance in Subunit IVb is moderate to severe, most commonly present as biscuiting and with some cracks.

Figure F10. XRD analyses, Site U1447. A. Serpentinite (lizardite) fragment from a coarse-sand bioclastic turbidite, Unit I. B. Foraminifer-rich nannofossil ooze with clay, Unit II. C, D. Bioclastic sand turbidite, Unit II.

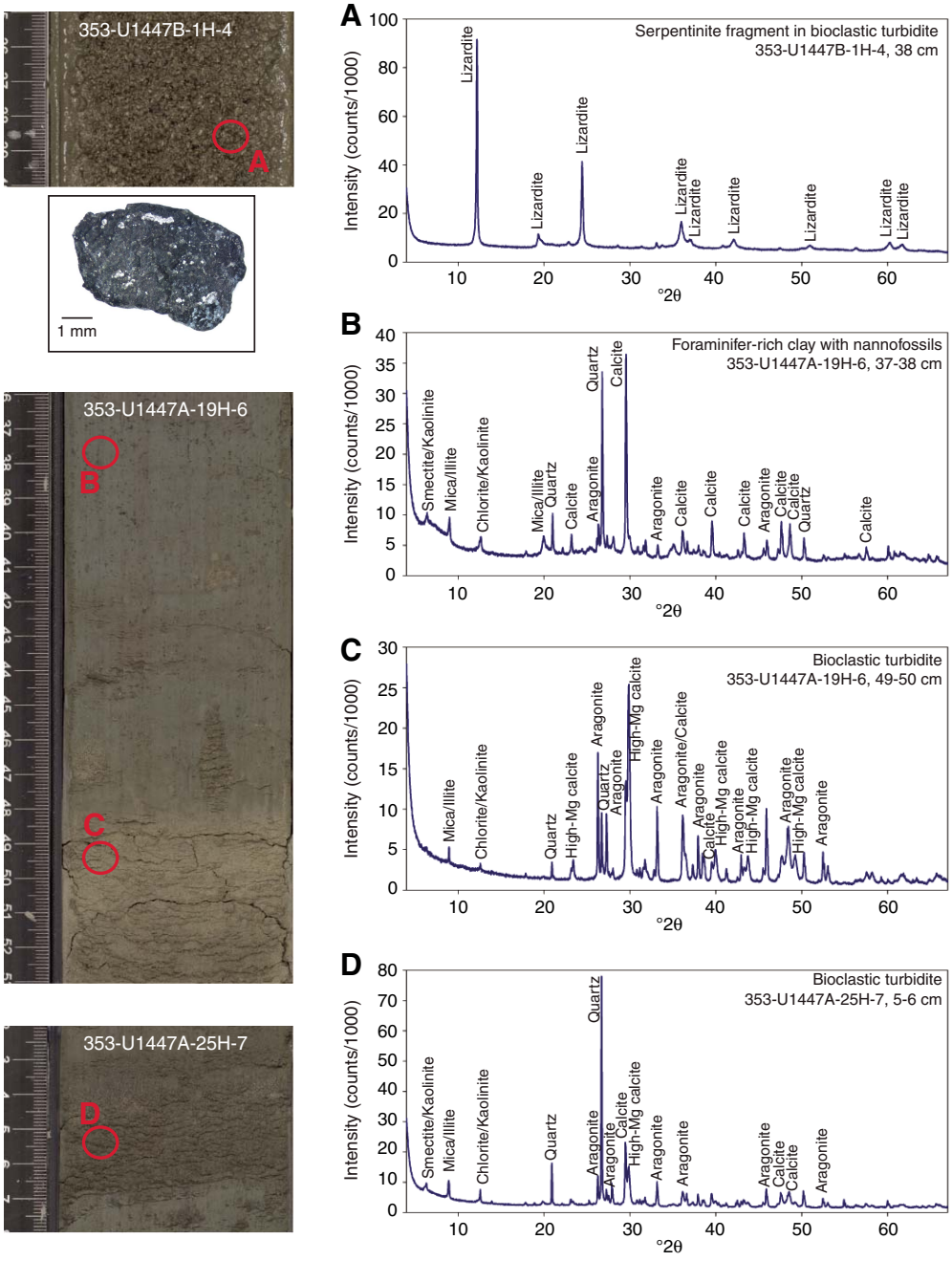

Figure F11. Turbidite abundance, thickness, and composition over the upper 400 m CSF-A, Hole U1447A (Units I and II). Qz = quartz.

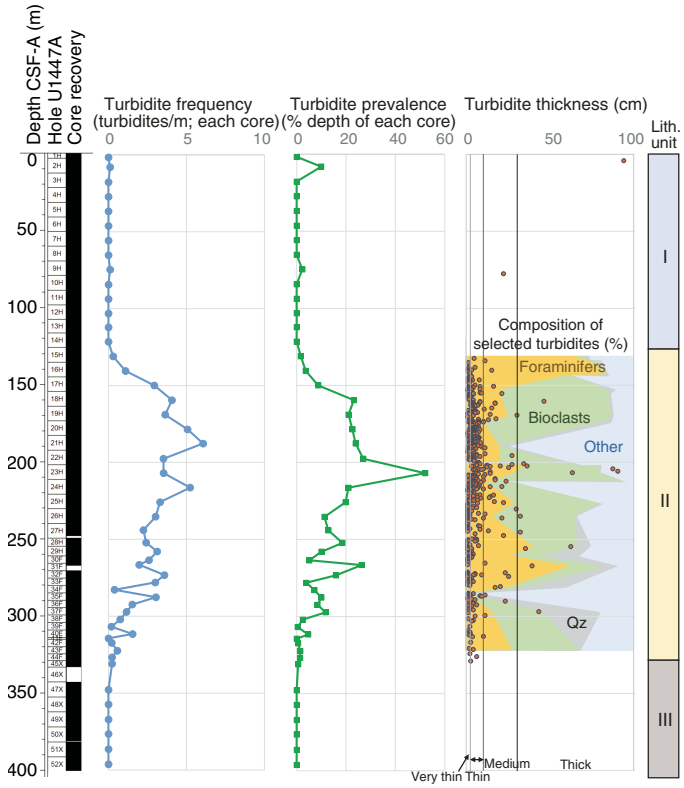

Biostratigraphy

Calcareous nannofossils are abundant (50%–90% of sediment particles) or common (10%–50%) throughout Hole U1447A. Their preservation is generally very good to moderate, except in Samples 353-U1447A-22H-CC and 23H-CC (202.69 and 211.88 m CSF-A), which contained poorly preserved overgrown nannofossils.

Foraminifers are dominant to abundant and very well preserved throughout the Pliocene and Pleistocene in Hole U1447A with a few exceptions in the turbiditic interval of lithostratigraphic Unit II, where preservation decreases to moderate or poor and/or abundance decreases to common. Foraminifers are dominant to abundant in most Miocene sediments as well, though abundance decreases to common or few in samples where diatom abundance is high. Preservation in the Miocene continues to be good with only two exceptions where moderate preservation accompanies low foraminifer abundances in Samples 353-U1447A-78X-CC and 88X-CC (651.57 and 740.44 m CSF-A, respectively).

Diatoms are sporadically present from 0 to 566 m CSF-A in Hole U1447A. Their abundance varies downcore between abundant and few between Samples 353-U1447A-71X-2W, 70–71 cm, and 88X-CC (576.67 and 740.44 m CSF-A). Valve preservation ranges from good to poor, and valves are better preserved whenever abundance is higher than common.

The age model for Hole U1447A was established by combining calcareous nannofossil, planktonic foraminifer, and diatom datums with paleomagnetic reversal datums. The oldest calcareous nannofossil sample studied (Sample 353-U1447A-88X-CC) contained *Discoaster hamatus*, suggesting an age greater than 9.53 Ma. The oldest planktonic foraminifer datum encountered is the first occurrence (FO) of *Neogloboquadrina acostaensis* (9.83 Ma) in Sample 86X-CC. *Globorotalia limbata* is found in Sample 87X-CC, suggesting that the basal age of Hole U1447A is between 9.83 and 10.66 Ma. The oldest diatom datum is the FO of *Thalassiosira burckliana* (between 719.87 and 721.31 m CSF-A), suggesting that the bottom of Hole U1447A is slightly older than 9.1 Ma.

Table T2. Semiquantitative calcareous nannofossils abundance counts from core catcher samples, Hole U1447A. **Download table in .csv format.**

Calcareous nannofossils

Calcareous nannofossils were examined in all core catcher samples from Hole U1447A. Additional split core samples from Hole U1447A were examined to refine the depth of biostratigraphic datums once they were defined between two core catcher samples. Semiquantitative species abundance estimates for all core catcher samples are shown in Table **T2**. Pleistocene to middle Miocene nannofossil assemblages are typical of tropical/subtropical paleoenvironments and include common *Florisphaera profunda, Gephyrocapsa* spp., *Reticulofenestra* spp., *Sphenolithus* spp., *Discoaster* spp., *Helicosphaera* spp., *Calcidiscus* spp., and *Umbilicosphaera* spp. This permitted the construction of a relatively high resolution stratigraphy using this fossil group (Table **T3**; Figure **F12**). In Samples 353-U1447A-22H-CC (202.69 m CSF-A) and 23H-CC (211.88 m CSF-A), the presence of abundant abiogenic carbonate particles (of detrital or authigenic origin) and a high degree of overgrowth of nannofossils prevented identification to species level. In all other samples studied, overgrowth of nannofossils was not significant under the light microscope and etching was minor, allowing species-level identification. Reworked species are few to common from the top of the hole to Sample 37F-CC (299.78 m CSF-A), below which they are few, rare, or not found (Table **T2**).

Pliocene–Pleistocene

Well-preserved calcareous nannofossils are present throughout the Pleistocene (approximately 0–300 m CSF-A) and Pliocene (approximately 300–470 m CSF-A) sedimentary section of Hole U1447A. All Pleistocene marker species defined by Martini (1971) and Okada and Bukry (1980) were found (Table **T3**) (**Biostratigraphy** in the Expedition 353 methods chapter [Clemens et al., 2016a] for zonal schemes used; all ages cited in the text and figures are those of Gradstein et al., 2012). *Emiliania huxleyi*, which delineates the base of Zone NN21 (0.29 Ma), is present in Sample 353-U1447A-6H-2W, 140 cm (44.2 m CSF-A), and in all shallower samples studied based on shipboard scanning electron microscope work.

The onset of the dominance of *E. huxleyi* among the Noelaerhabdaceae could not be determined because this species is common down to Sample 353-U1447A-5H-CC (41.65 m CSF-A), just above where its FO was recorded. The last occurrence (LO) of *Pseudoemiliania lacunosa*, dated at 0.44 Ma, occurs between Samples 8H-CC and 9H-CC (midpoint depth = 74.81 m CSF-A). *Reticulofenestra asanoi* is present in Samples 13H-CC through 16H-CC (116.47–145.52 m CSF-A). Similar to other IODP Expedition 353 sites, the only large (>5.5 µm) *Gephyrocapsa* coccoliths found were present in the Late Pleistocene and belonged to the species *Gephyrocapsa oceanica*. Other well-defined Pleistocene events at Site U1447 are the FOs of *Helicosphaera sellii, Calcidiscus macintyrei, Discoaster brouweri, Discoaster triradiatus*, and *Discoaster pen-*

Table T3. Calcareous nannofossil datums, Hole U1447A. * = boundary ages of Subzone CN9c, corresponding to Subzone NN11c, containing the entire range of the species (Bown, 1998). B = bottom, T = top, Bc = bottom common. GTS2012 = Geologic Timescale 2012. **Download table in .csv format.**

Species event	GTS2012 age (Ma)	Site	Hole	Top				Bottom				Midpoint depth CSF-A (m)	Depth ± (m)
				Core	Section	Interval (cm)	Depth CSF-A (m)	Core	Section	Interval (cm)	Depth CSF-A (m)		
B *Emiliania huxleyi*	0.29	U1447	A	6H	2W	140	44.2	6H	4W	140	47.17	45.69	1.49
T *Pseudoemiliania lacunosa*	0.44	U1447	A	8H	CC		70.105	9H	CC		79.52	74.81	4.70
Bc *Reticulofenestra asanoi*	1.14	U1447	A	16H	CC		145.545	17H	CC		154.85	150.20	4.65
T *Helicosphaera sellii*	1.26	U1447	A	19H	3W	15	167.01	19H	5W	15	169.87	168.44	1.43
T *Calcidiscus macintyrei*	1.6	U1447	A	25H	3W	15	224.03	25H	5W	15	227.05	225.54	1.51
T *Discoaster brouweri*	1.93	U1447	A	28H	CC	254.855	254.855	29H	5W	38	260.65	257.75	2.90
T *Discoaster triradiatus*	1.95	U1447	A	29H	5W	38	260.65	29H	CC		260.91	260.78	0.13
T *Discoaster pentaradiatus*	2.39	U1447	A	37F	CC	299.775	299.775	38F	2W	100	301.89	300.83	1.06
Pliocene/Pleistocene boundary	2.59												
T *Sphenolithus* spp.	3.54	U1447	A	48X	CC		362.195	49X	3W	50	365.71	363.95	1.76
T *Reticulofenestra pseudoumbilicus*	3.7	U1447	A	50X	4W	100	377.4	50X	CC		381.10	379.25	1.85
T *Ceratolithus acutus*	5.04	U1447	A	56X	4W	100	435.6	56X	CC		439.00	437.30	1.70
B *Ceratolithus cristatus*	5.12	U1447	A	57X	2W	50	441.8	57X	4W	100	445.30	443.55	1.75
T *Triquetrorhabdulus rugosus*	5.28	U1447	A	59X	CC		468.885	60X	2W	110	471.50	470.19	1.31
Pliocene/Miocene boundary	5.33												
B *Ceratolithus acutus*	5.35	U1447	A	59X	CC		468.885	60X	2W	110	471.50	470.19	1.31
T *Discoaster quinqueramus*	5.59	U1447	A	59X	CC		468.885	60X	2W	110	471.50	470.19	1.31
T *Reticulofenestra rotaria*	5.94*	U1447	A	67X	CC		546.365	68X	CC		556.465	551.42	5.05
B *Reticulofenestra rotaria*	6.91*	U1447	A	71X	CC		585.305	72X	CC		594.925	590.12	4.81
B *Discoaster quinqueramus*	8.12	U1447	A	78X	2W	84	645.84	78X	4W	84	648.84	647.34	1.50
B *Discoaster berggrenii*	8.29	U1447	A	79X	3W	127	651.98	79X	CC		653.89	652.94	0.95
T *Minylitha convallis*	8.68	U1447	A	82X	3W	20	674.66	81X	CC		682.47	678.57	3.91
T *Discoaster hamatus*	9.53	U1447	A	85X	CC		711.425	86X	CC		721.29	716.355	4.93

taradiatus (Table **T3**; Figure **F12**). We note that in Hole U1447A, *D. triradiatus* is rare where present; therefore, limited confidence can be placed in the exact depths of its LO at 1.95 Ma.

The Pliocene/Pleistocene boundary (2.59 Ma) is placed just below the LO of *D. pentaradiatus* (2.39 Ma), which occurs between Samples 353-U1447A-37F-CC and 38F-2W, 100 cm (299.78 and 301.89 m CSF-A). The LO of *Sphenolithus* species (3.54 Ma) occurs between Samples 48X-CC and 49X-3W, 50 cm. *Reticulofenestra pseudoumbilicus* (>7 µm) was found in Sample 50X-CC (381.10 m CSF-A) and deeper. *Discoaster asymmetricus* was almost entirely absent from the Site U1447 assemblage.

Miocene

The Miocene/Pliocene boundary (5.33 Ma) occurs between Samples 353-U1447A-59X-CC and 60X-2W, 110 cm (468.89 and 470.19 m CSF-A), based on the LO of *Triquetrorhabdulus rugosus* (5.28 Ma) and the FO of *Ceratolithus acutus* (5.35 Ma) in this interval. The LO of *Discoaster quinqueramus* (5.59 Ma) also occurs between the same samples. *Reticulofenestra rotaria*, which occurs in Subzone CN9c (Bown, 1998) (5.94 to 6.91 Ma based on the calibrated ages of Gradstein et al., 2012), was present in Samples 68X-CC through 71X-CC (556.47–585.31 m CSF-A). The FOs of *D. quinqueramus* (8.12 Ma) and *Discoaster berggrenii* (8.29 Ma) occurred between Samples 78X-2W, 84 cm, and 79X-CC (645.84 and 653.89 m CSF-A). *Minylitha convallis* occurs in Sample 82X-CC (682.47 m CSF-A) and deeper. The oldest sample studied for biostratigraphy (Sample 88X-CC; 740.44 m CSF-A) contains *D. hamatus*, suggesting an age greater than 9.53 Ma.

Planktonic foraminifers

Planktonic foraminifer biostratigraphy of the Pleistocene to late Miocene section of Site U1447 was based on the shipboard study of core catcher samples from Hole U1447A with the addition of a single sample from Section 353-U1447A-47X-1W. Planktonic foraminifer distribution in Hole U1447A is shown in Table **T4**. The absolute ages assigned to biostratigraphic datums listed in Table **T5** follow the references given in Table **T2** in the Expedition 353 methods chapter (Clemens et al., 2016a).

Planktonic foraminifer percentage is consistently high (mean = 93.6%) in the Pliocene and Pleistocene, though two samples in the turbiditic interval (Unit II) show considerably lower values: 47.5% in Sample 353-U1447A-22H-CC (202.69 m CSF-A) and 68.1% in Sample 31F-CC (267.28 m CSF-A). Planktonic foraminifer percentage is more variable in the Miocene, as it and the total number of foraminifers per 10 cm^3 decreases as diatom abundance increases. The planktonic/benthic ratio, reported as percentage planktonic foraminifers of the total foraminifer population, and the number of benthic foraminifers and total foraminifers found in a 10 cm^3 sample are based on examination of the >150 µm size fraction of core catcher samples.

Pleistocene

Pleistocene planktonic foraminifer assemblages were recovered from Samples 353-U1447A-1H-CC through 34F-CC (3.35 to 285.36 m CSF-A). Foraminifers are dominant and very well preserved with few exceptions in the turbiditic interval where preservation decreases to moderate or poor and/or abundance decreases to abundant or common. Planktonic assemblages are dominated by the tropical to warm subtropical species *Globigerinoides ruber, Neogloboquadrina dutertrei, Pulleniatina obliquiloculata*, and *Globigerinoides sacculifer.*

The LO of *G. ruber* (pink) in Sample 353-U1447A-4H-CC (32.26 m CSF-A) places these sediments in Zone PT1b. The top of Zone PT1a is located at the LO of *Globorotalia tosaensis* in Sample 11H-CC (98.79 m CSF-A). The LOs of *Globigerinoides obliquus* in Sample 18H-CC (164.54 m CSF-A), *N. acostaensis* in Sample 24H-CC (221.22 m CSF-A), and *Globigerinoides fistulosus* in Sample 26H-CC (240.08 m CSF-A) define Zone PT1a. The LO of *Globoturborotalita woodi* in Sample 35F-CC (290.24 m CSF-A) defines the base of Zone PL6.

Figure F12. Summary of biostratigraphic events identified in Hole U1447A. T = top (last occurrence), B = bottom (first occurrence), Tc = top common, Bc = base common, FO = first occurrence, LO = last occurrence. For biozone schemes used, see **Biostratigraphy** in the Expedition 353 methods chapter (Clemens et al., 2016a).

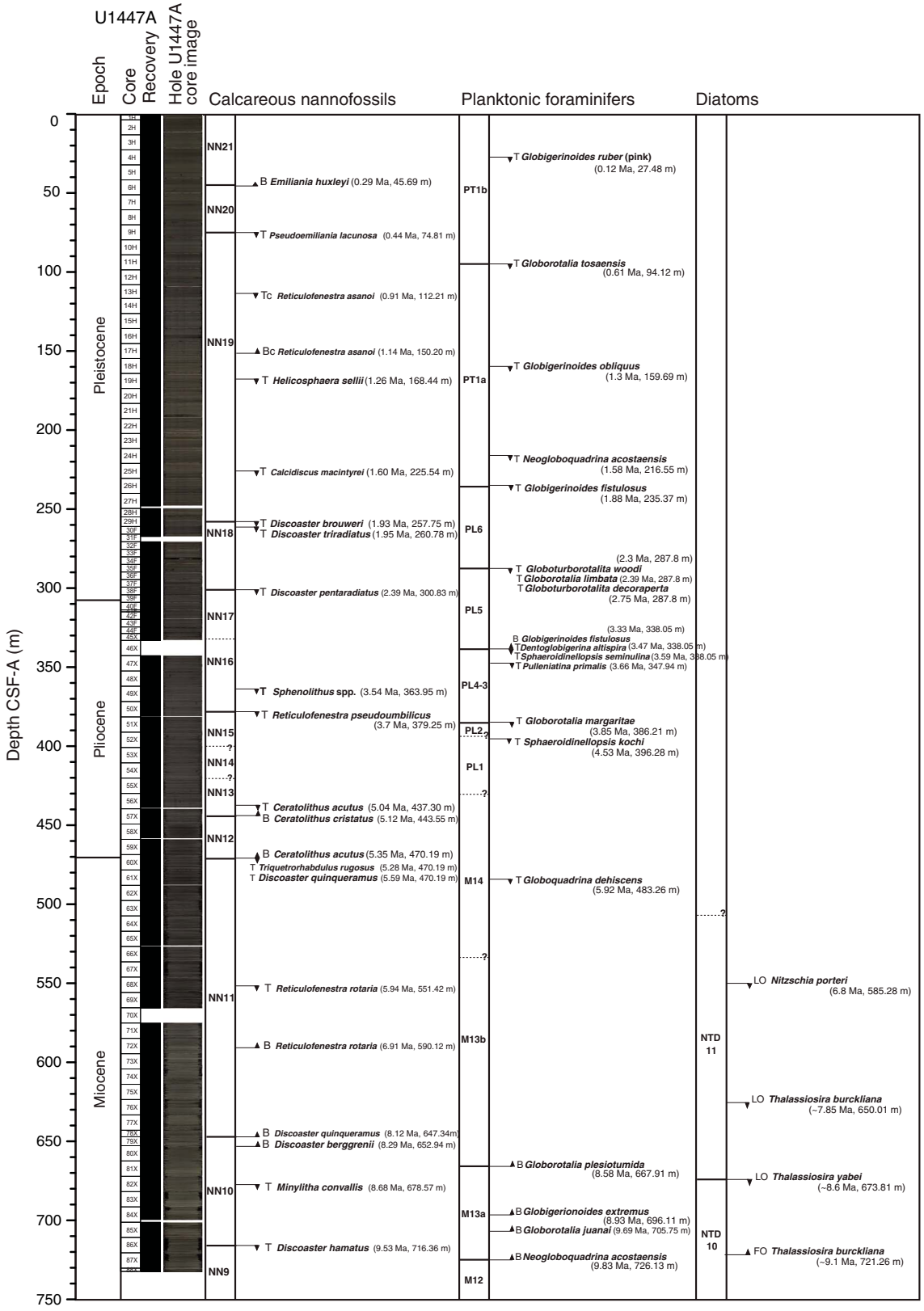

Table T4. Semiquantitative planktonic foraminifer abundance counts from core catcher samples, Hole U1447A. **Download table in .csv format.**

Table T5. Planktonic foraminifer datums, Hole U1447A. T = top, B = bottom. GTS2012 = Geologic Timescale 2012. **Download table in .csv format.**

Core, section, interval (cm)		Zone	Marker event	GTS2012 age (Ma)	Depth CSF-A (m)			Depth ± (m)
Top	Bottom				Top	Bottom	Midpoint	
353-U1447A-	353-U1447A-							
3H-CC	4H-CC	PT1b	T *Globigerinoides ruber* (pink); Indo-Pacific	0.12	22.71	32.26	27.49	4.77
10H-CC	11H-CC	PT1b/PT1a	T *Globorotalia tosaensis*	0.61	89.46	98.79	94.13	4.67
17H-CC	18H-CC	PT1a	T *Globigerinoides obliquus*	1.30	154.85	164.54	159.70	4.84
23H-CC	24H-CC	PT1a	T *Neogloboquadrina acostaensis*	1.58	211.88	221.22	216.55	4.67
25H-CC	26H-CC	PT1a	T *Globigerinoides fistulosus*	1.88	230.66	240.08	235.37	4.71
34F-CC	35F-CC	PL6	T *Globoturborotalita woodi*	2.30	285.36	290.24	287.80	2.44
34F-CC	35F-CC	PL5	T *Globorotalia limbata*	2.39	285.36	290.24	287.80	2.44
		Pleistocene/Pliocene boundary		2.59				
34F-CC	35F-CC	PL5	T *Globoturborotalita decoraperta*	2.75	285.36	290.24	287.80	2.44
45X-CC	47X-1, 20–24	PL5	B *Globigerinoides fistulosus*	3.33	333.08	343	338.04	4.96
45X-CC	47X-1, 20–24	PL5/PL4	T *Dentoglobigerina altispira* (Pacific)	3.47	333.08	343	338.04	4.96
45X-CC	47X-1, 20–24	PL4/PL3	T *Sphaeroidinellopsis seminulina* (Pacific)	3.59	333.08	343	338.04	4.96
47X-1, 20–24	47X-CC	PL3	T *Pulleniatina primalis*	3.66	343.04	352.87	347.96	4.91
50X-CC	51X-CC	PL3/PL2	T *Globorotalia margaritae*	3.85	381.10	391.33	386.22	5.11
51X-CC	52X-CC	PL1	T *Sphaeroidinellopsis kochi*	4.53	391.33	401.24	396.29	4.96
		Pliocene/Miocene boundary		5.33				
60X-CC	61X-CC	M14	T *Globoquadrina dehiscens*	5.92	478.51	488.02	483.27	4.75
80X-CC	81X-CC	M13b	B *Globorotalia plesiotumida*	8.58	663.29	672.54	667.92	4.63
83X-CC	84X-CC	M13a	B *Globigerinoides extremus*	8.93	692.15	700.08	696.12	3.97
84X-CC	85X-CC	M13a	B *Globorotalia juanai*	9.69	700.08	711.43	705.76	5.67
86X-CC	87X-CC	M13a	B *Neogloboquadrina acostaensis*	9.83	721.29	730.98	726.14	4.85

Pliocene

Pliocene planktonic foraminifer assemblages were recovered from Samples 353-U1447A-35F-CC through 60X-CC (290.24–478.51 m CSF-A). Foraminifers are dominant to abundant and very well preserved except where preservation decreases to moderate in the turbiditic interval. *G. sacculifer, G. ruber, Globigerinoides extremus, Dentoglobigerina altispira, Globigerinoides trilobus*, and *N. dutertrei* dominate Pliocene samples.

The LO of *G. limbata* is found in Sample 353-U1447A-35F-CC (290.24 m CSF-A), marking the top of Zone PL5. The LO of *Globoturborotalita decoraperta* in Sample 35F-CC (290.24 m CSF-A) and the FO of *G. fistulosus* in Sample 45X-CC (333.08 m CSF-A) further define Zone PL5. The LO of *D. altispira* in Sample 47X-1W, 20–24 cm (343.02 m CSF-A), defines the upper boundary of Zone PL4. The LO of *Sphaeroidinellopsis seminulina* in this same sample marks the top of Zone PL3, such that Zone PL4 is not represented in these sediments. The LO of *Pulleniatina primalis* within Zone PL3 is in Sample 47X-CC (352.87 m CSF-A). The upper boundary of Zone PL2 is marked by the LO of *Globorotalia margaritae* in Sample 51X-CC (391.33 m CSF-A), and the LO of *Sphaeroidinellopsis kochi* in Sample 52X-CC (401.24 m CSF-A) marks the top of Zone PL1.

Miocene

Samples 353-U1447A-61X-CC through 88X-CC (488.02–740.44 m CSF-A) contain Miocene sediments. Foraminifers are dominant to abundant in most samples, though abundance decreases to common or few where diatom abundance is high. Preservation is good with only two exceptions where moderate preservation accompanies low foraminifer abundances in Samples 78X-CC and 88X-CC.

The planktonic foraminifer assemblage is dominated by *G. trilobus, G. obliquus*, and *G. extremus*. *Globorotalia menardii* appears sporadically as a common to abundant member of the assemblage. The LO of *Globoquadrina dehiscens* in Sample 353-U1447A-61X-CC (488.02 m CSF-A) identifies Zone M14, and the FO of *Globorotalia plesiotumida* in Sample 80X-CC (663.29 m CSF-A) identifies Zone M13b. The M14/M13b boundary could not be resolved. The FOs of *G. extremus* in Sample 83X-CC (692.15 m CSF-A) and *Globorotalia juanai* in Sample 84X-CC (700.08 m CSF-A) mark these samples as part of Zone M13a. The FO of *N. acostaensis* (Zone M13a; 9.83 Ma) is found in Sample 86X-CC. *G. limbata* is found in Sample 87X-CC, suggesting that the basal age of Hole U1447A is between 9.83 and 10.66 Ma. Sample 88X-CC (740.44 m CSF-A) contained few foraminifers, and an age diagnosis was not possible.

Table T6. Semiquantitative diatom abundance counts from core catcher and split core samples, Site U1447. **Download table in .csv format.**

Diatoms

In order to define the sediment age and paleoenvironmental conditions, core catcher samples and samples from selected split core sections from Hole U1447A were investigated. The sampling resolution was high, and the number of samples studied for each core varied between 2 and 6. The distribution of diatoms in Hole U1447A is shown in Table **T6**. The absolute ages assigned to biostratigraphic datums listed in Table **T7** follow the references given in Table **T3** in the Expedition 353 methods chapter (Clemens et al., 2016a). Figure **F13** shows the age/depth plot for Site U1447 (also shown are calcareous nannofossils and foraminifer datums).

The diatom community at Site U1447 is highly diverse and mainly consists of species typical of warm to temperate low-latitude ocean waters. High-productivity water species, including *Thalassionema nitzschioides* var. *nitzschioides* and *Cyclotella striata*, tend to dominate when total diatom abundance is higher than "few" in the uppermost 53 m. Accompanying components of the diatom assemblage are warm and temperate species including *Azpeitia nodulifera, Shionodiscus oestrupii*, and *Alveus marinus*. Deeper than 556.11 m CSF-A in Hole U1447A, *T. nitzschioides* and *Thalassiothrix* spp. dominate, whereas *T. burckliana, Nitzschia porteri, Paralia sulcata, Actinoptychus senarius*, and *Azpeitia nodulifera* fa. *cyclopa* are secondary components.

Table T7. Diatom datums, Site U1447. LO = last occurrence, FO = first occurrence. * = see the **Expedition 353 methods** chapter (Clemens et al., 2016a) for references. **Download table in .csv format.**

Species event	Calibrated age* (Ma)	Site	Hole	Top Core	Top Section	Top Interval (cm)	Top Depth CSF-A (m)	Bottom Core	Bottom Section	Bottom Interval (cm)	Bottom Depth CSF-A (m)	Midpoint depth CSF-A (m)
Miocene												
LO *Nitzschia porteri*	6.8	U1447	A	71X	CC	0–5	585.31	72X	2W	76–76	587.56	586.42
FO *Nitzschia reinholdii*	?	U1447	A	74X	6W	66–66	612.90	74X	CC	0–5	614.87	613.90
LO *Thalassiosira burckliana*	7.85	U1447	A	79X	2W	80–80	650.01	79X	3W	76–76	651.47	650.74
LO *Thalassiosira yabei*	8.6	U1447	A	82X	2W	76–76	673.81	82X	CC	0–5	682.47	678.15
FO *Thalassiosira burckliana*	9.1	U1447	A	86X	CC	0–5	721.29	87X	2W	45–45	723.15	722.21

Figure F13. Biostratigraphic- and magnetostratigraphic-based age-depth plot, Hole U1447A. Vertical error bars show the depth range of the identified biostratigraphic events (e.g., between two core catchers or two core sections). Color shading along the *x*-axis shows the ages of the Pleistocene, Pliocene and Miocene. For magnetostratigraphy, the two different symbols represent ages determined using Class 1 (more conservative) and Class 2 data sets. See **Magnetostratigraphy** for more discussion.

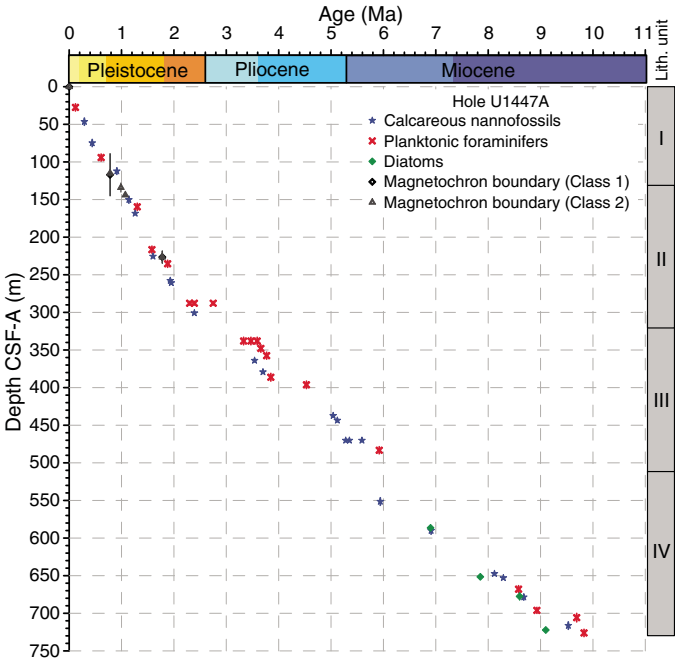

Diatom biostratigraphy

Diatoms are useful for age estimation deeper than 556.11 m CSF-A in Hole U1447A. The co-occurrence of *Nitzschia reinholdii* and *N. porteri* between Samples 353-U1447A-72X-2W, 76 cm, and 74X-6W, 66 cm (587.56 and 612.9 m CSF-A), delimits this interval to a subzone of the *Nitzschia miocenica* Zone (see Table **T3** in the Expedition 353 methods chapter [Clemens et al., 2016a]). The LO of *N. porteri* (6.8 Ma) was observed between Samples 71X-CC and 72X-2W, 76 cm (585.31 and 587.56 m CSF-A). Close to this bioevent, the FO of *N. reinholdii* was found between Samples 74X-6W, 66 cm, and 74X-CC (612.90 and 614.87 m CSF-A). The LO of *T. burckliana* (7.85 Ma) was found between Samples 79X-2W, 80 cm, and 79X-3W, 76 cm (650.01 and 651.47 m CSF-A): this bioevent divides the *N. porteri* Zone (NTD11) into Subzones a and b. The LO of *Thalassiosira yabei* (8.6 Ma) defines the boundary between the *N. porteri* (NTD11) and *T. yabei* (NTD10) Zones and was found between Samples 82X-2W, 76 cm, and 82X-CC (673.81 and 682.47 m CSF-A). Finally, the FO of *T. burckliana* between Samples 86X-CC and 87X-2W, 45 cm (721.29 and 723.15 m CSF-A), defines the boundary between Subzones a and b of the *Thalassiosira yabei* Zone. This event suggests that the bottom of Hole U1447A is slightly older than 9.1 Ma.

Sedimentation rates and age model

Age-depth relationships for Hole U1447A based on biostratigraphy for the three fossil groups studied (calcareous nannofossils, planktonic foraminifers, and diatoms) show good agreement (Figure **F13**). A few paleomagnetic reversals were also determined at Site U1447 (see **Magnetostratigraphy**). The match between biostratigraphic datums and magnetochron boundary datums is very good. Based on linear fits including all data, sedimentation rates in Hole U1447A are relatively high in the Pleistocene (on average 12 cm/ky linear sedimentation rate [LSR]) and moderate in the Pliocene and most of the Miocene (on average 6.5 cm/ky LSR). The sedimentation rate deeper than 700 m CSF-A decreases to about 3.3 cm/ky; however, only limited confidence can be placed in this observation, as it is based on few data points (Figure **F13**). A number of unconformities with possible short-term stratigraphic hiatuses are indicated in Figure **F13** by the co-occurrence of three or more successive biostratigraphic events within the same stratigraphic interval (e.g., 290, 340, 470, and 650 m CSF-A). Some of these events are associated with observed lithologic changes or features (see the **Expedition 353 summary** chapter [Clemens et al., 2016b]).

Geochemistry

The geochemistry of Site U1447 mainly reflects the anaerobic processes of sulfate reduction and methanogenesis associated with microbial degradation of organic matter. The organic carbon content ranges from 0.1 to 2.0 wt% (average = 0.8 wt%). Sulfate declines rapidly from 28 mM at the sediment/water interface to nearly zero at approximately 20 m CSF-A. Alkalinity peaks at 20 m CSF-A, consistent with the production of bicarbonate during sulfate reduction. A gradual increase in dissolved Ba concentration with depth suggests ongoing barite dissolution and potential deep sulfate reduction. Changes in the concentrations of other elements and ions (Fe, Mn, Ca, B, ammonia, and Sr) in interstitial water can be readily explained by microbially mediated chemical reactions and their effects on pH, alkalinity, and mineral dissolution and precipitation. Headspace methane concentration peaks at 125 m CSF-A, abruptly decreases below the peak, and is consistently low to the bottom of the hole. High methane/ethane ratios suggest that the methane is mostly of biogenic origin (methanogenesis). Carbonate content varies significantly between 9 and 55 wt%.

Sediment gas sampling and analysis

Headspace gas samples were taken at a frequency of one sample per core in Hole U1447A as part of the routine environmental protection and safety-monitoring program (Table **T8**). Methane concentration increases from around 2 parts per million (ppm) in the upper 22 m CSF-A to a peak of 345 ppm at 69 m CSF-A, followed by a larger peak of 1065 ppm at 125 m CSF-A, before decreasing to <140 ppm from 144 m CSF-A until the bottom of the hole (Figure **F14**). Heavier hydrocarbons such as ethane and propane were not detected. Void gas analysis indicates a trace amount of ethane, but the methane/ethane ratio is higher than 14,000 (Table **T9**), which suggests that methane is of biogenic origin. Ethane and hydrogen sulfide were also detected in void gas samples. In Hole U1447B, headspace gas samples were taken at a frequency of one per section as part of high-resolution geochemical studies in the uppermost 25 m (Table **T8**). Methane concentrations are low throughout (<2 ppm), consistent with results from Hole U1447A.

Bulk sediment geochemistry

Calcium carbonate, inorganic carbon, and total organic carbon (TOC) contents were determined on sediment samples from Hole U1447A (Table **T10**; Figure **F15**). $CaCO_3$ concentration ranges between 9 and 55 wt% and is highest in the upper part of lithostratigraphic Unit II, which corresponds to carbonate turbidites, and lithostratigraphic Subunit IVb (Figure **F15**). TOC ranges between 0.1 and 2.0 wt% and is highest within lithostratigraphic Unit II.

Table T8. Headspace methane concentrations, Site U1447. **Download table in .csv format.**

Figure F14. Headspace methane concentrations and void gas methane, ethane, and hydrogen sulfide concentrations, Hole U1447A.

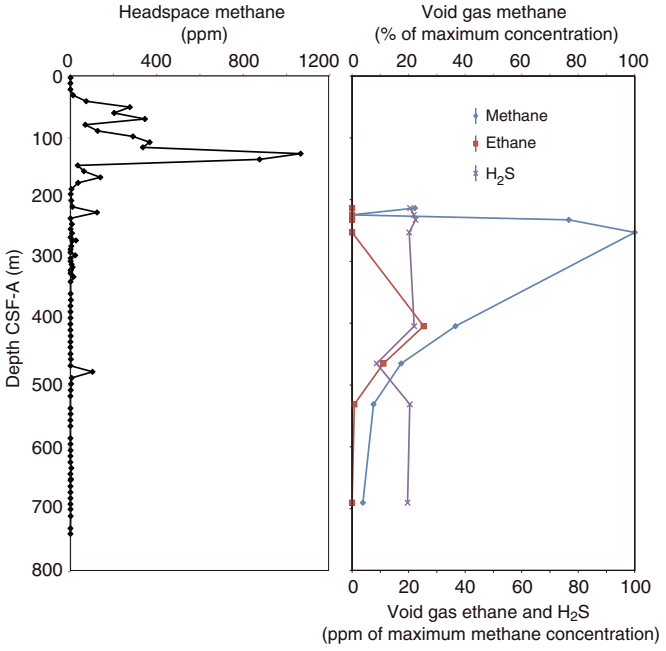

Table T9. Void gas methane, ethane, and hydrogen sulfide concentrations, Hole U1447A. **Download table in .csv format.**

Table T10. Calcium carbonate and carbon contents, Hole U1447A. **Download table in .csv format.**

Interstitial water sampling and chemistry

Hole U1447A was analyzed for pore water chemistry at a relatively coarse resolution of one sample per core for all cores. Hole U1447B was sampled for high-resolution geochemistry at a resolution of one sample per section (150 cm) for three cores (i.e., the top 25 m CSF-A). Most whole-round samples for pore water squeezing were kept under N_2 before and during extraction of interstitial waters, and some additional samples were taken using Rhizon samplers (Table **T11**).

Concomitant with a sharp drawdown of sulfate in the uppermost 20 m, alkalinity increases (Figure **F16**; Table **T11**). Although sulfate is below detection from ~20 m CSF-A downhole, Ba increases sharply from a few micromolar at ~11 m CSF-A to ~67 µM at ~21 m CSF-A. Alkalinity peaks at ~34 mM at 30 m CSF-A, slowly decreases to ~11 mM at 190 m CSF-A, and varies between ~11 and 14 mM for the rest of the sediment section. The alkalinity change deeper than 20 m CSF-A is more difficult to explain but is likely related to the varying production-consumption balance of various anaerobic microbial processes.

Ammonium increases from 0.4 mM at the top of Hole U1447B to 5.8 mM at 200 m CSF-A in Hole U1447A (Figure **F16**). The ammonium increase rate in the uppermost 30 m is roughly twice as fast as that deeper than 30 m CSF-A. Dissolved Mn concentration decreases rapidly from 0 to ~21 m CSF-A from 31 to 4.27 µM, consistent with microbial reduction of Mn oxides in the uppermost sediments (Figure **F16**; Table **T11**). Although dissolved Fe decreases from 12 to ~3 µM within the uppermost 20 m of the sediment column, it varies between ~2 and 51 µM in the remaining sediment column, probably reflecting variable amounts and dissolution of residual Fe oxides in sediments. When associated with sulfate reduction and production of hydrogen sulfide, soluble Fe is scavenged by sulfide and converted to sulfide minerals and eventually pyrite. Calcium concentration decreases from around 10 mM near the sediment/water interface to ~2.5 mM at ~20 m CSF-A then

Figure F15. Calcium carbonate and TOC contents, Hole U1447A.

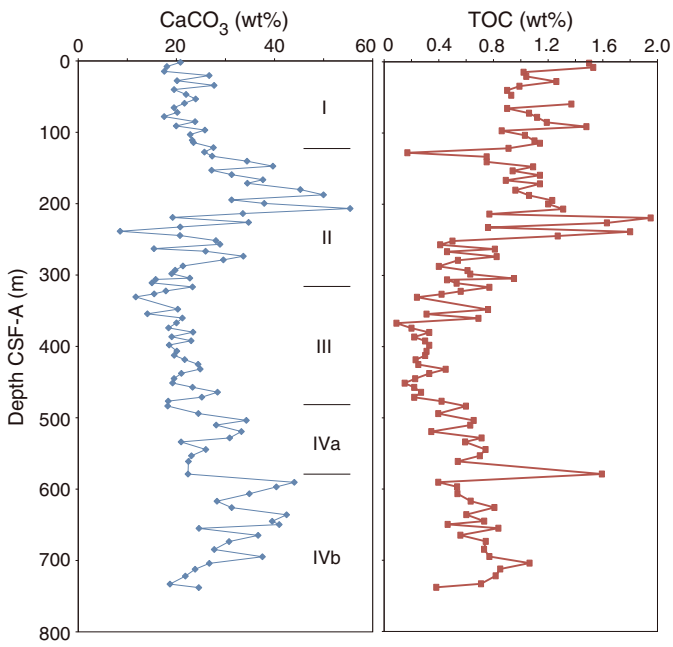

Table T11. Interstitial water chemistry, Holes U1447A and U1447B. **Download table in .csv format.**

Figure F16. Pore water alkalinity, Ba, SO_4^{2-}, Li, Fe^{2+}, Mn, NH_4^+, Br, Ca, Mg, K, B, Sr, and Si, Holes U1447A and U1447B. Error bars represent two standard deviations of repeated measurements of IAPSO seawater or a pore water sample (see **Geochemistry** and Tables **T5**, **T6**, all in the Expedition 353 methods chapter [Clemens et al., 2016a]).

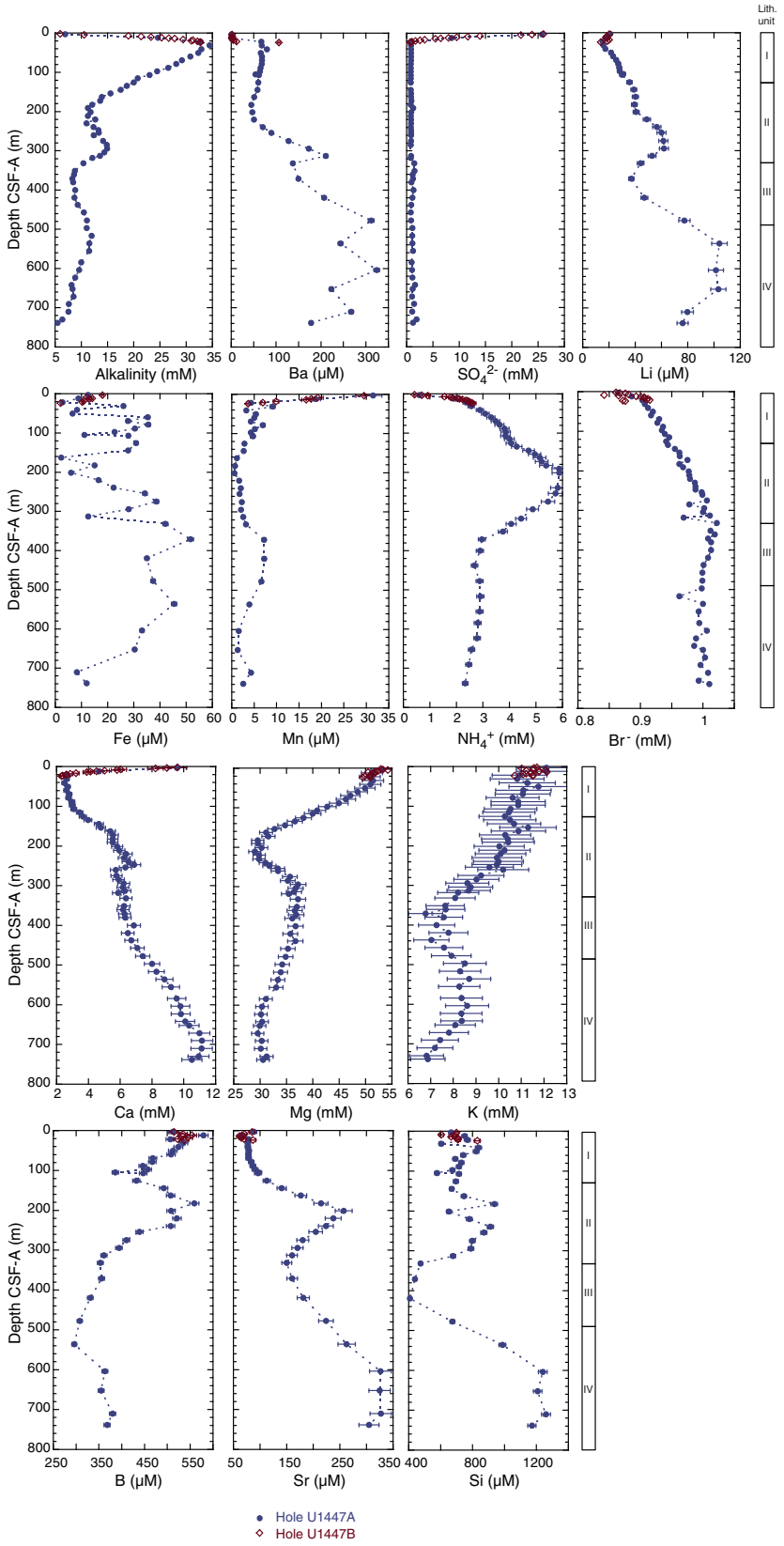

increases with depth with a break in slope at ~250 m CSF-A. The drop in Ca concentration in the uppermost 20 m is most likely related to the production of bicarbonate with sulfate reduction and carbonate precipitation. Magnesium is highest at ~4 m CSF-A and gradually decreases to a minimum of 30 mM around 200 m CSF-A. Deeper than 200 m CSF-A, Mg increases to ~36 mM at ~300 m CSF-A before decreasing to around 30 mM toward the bottom of the hole.

Boron concentration decreases from around 550 µM at 0 m CSF-A to 350 µM at 100 m CSF-A (Figure **F16**; Table **T11**) before peaking at around 550 µM near 200 m CSF-A. Deeper than 200 m CSF-A, B decreases with depth and fluctuates between 296 and 380 µM. Interestingly, Li, Si, and Sr all show similar downhole patterns with a peak around 300 m CSF-A, followed by a trough and increase to a flat-topped peak deeper than 600 m CSF-A. The minimum and maximum concentrations of Li, Sr, and Si are 15, 66, and 408 and 107, 326, and 1260 µM, respectively (Figure **F16**; Table **T11**).

Paleomagnetism

Paleomagnetic measurements were conducted on archive-half sections for all three holes at Site U1447 with alternating field (AF) demagnetization up to 10 mT (Figures **F17**, **F18**). Discrete samples taken from the working-half sections of Hole U1447A (N = 200) were also analyzed with AF demagnetization between 40 and 80 mT (Table **T12**). Characteristic remanent magnetization (ChRM) of these discrete samples was calculated using the principal component analysis (PCA) technique. In addition, anhysteretic remanent magnetization (ARM) was acquired and measured on a selection of discrete samples from Hole U1447A for preliminary insight into depth variations in Site U1447 sediment bulk magnetic properties.

Magnetostratigraphy

Cores 353-U1447A-2H through 29H and 353-U1447C-4H through 15H were oriented using the Icefield MI-5 tool. Therefore we have obtained "true" declinations between 3.30 and 260.2 m CSF-A for Hole U1447A and 18.4 and 133.45 m CSF-A for Hole U1447C (Figures **F17**, **F18**). For some cores, the orientation tool was not stable before shooting, and the orientation pick is somewhat subjective (Table **T13**). Nonetheless, the true declinations reasonably concentrate around 0 (360°) downhole to ~90 m CSF-A for both holes, indicating normal magnetic polarity. Deeper than ~90 m CSF-A, scatter in declination starts to increase, introducing uncertainty in polarity determinations. Declination data between ~140 and 220 m CSF-A from Hole U1447A seem to concentrate around 180°, and we argue that this interval shows reversed polarity. Inclination after 10 mT becomes steeper deeper than ~90 m CSF-A for both Holes U1447A and U1447C, suggesting more severe drilling-related overprint. Similar to the section measurements, discrete samples revealed reasonable ChRM downhole to ~90 m CSF-A

Figure F17. Downhole variations in declination, inclination, and intensity, Hole U1447A. Gray and black symbols = before and after 10 mT AF demagnetization, respectively.

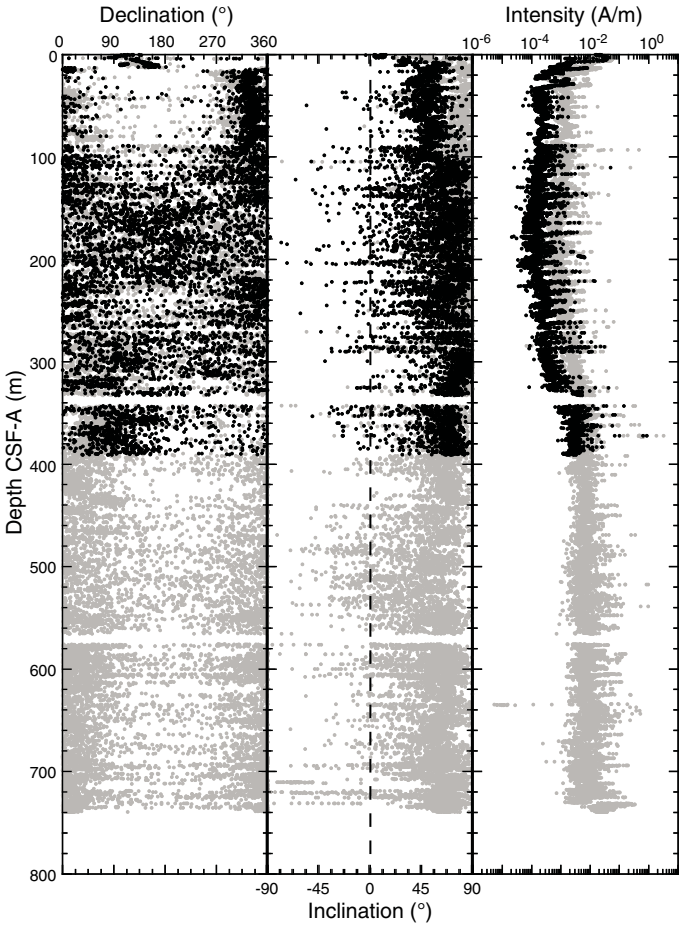

Figure F18. Downhole variations in declination, inclination, and intensity, Hole U1447C. Gray and black symbols = before and after 10 mT AF demagnetization, respectively.

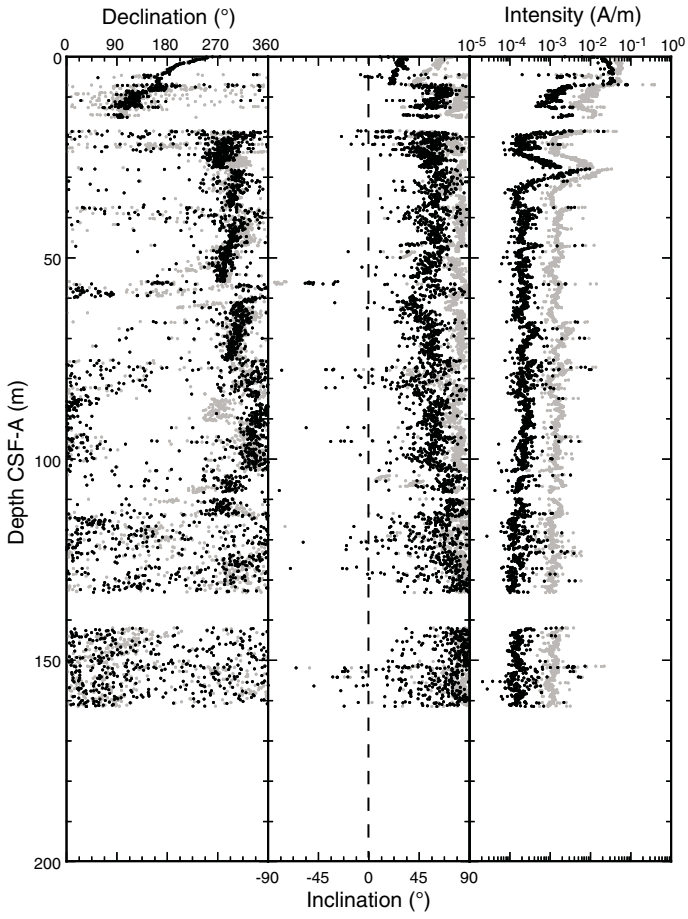

Table T12. Summary of discrete sample measurements, Hole U1447A. AF = alternating field, PCA = principal component analysis, MAD = maximum angular deviation. (Continued on next two pages.) **Download table in .csv format.**

Core	Type	Section	Top offset (cm)	Top depth CSF-A (m)	NRM (A/m)	Inclination (AF 10 mT) (°)	Declination (AF 10 mT) (°)	True declination (AF 10 mT) (°)	PCA inclination (°)	True PCA declination (°)	PCA MAD1 (°)	PCA MAD3 (°)	PCA anchored	PCA start (mT)	PCA end (mT)
1	H	1	100	1	0.03458	8.2			10.2		3.2	2.9	Y	0	80
1	H	2	55	2.05	0.0377	13.1			12.2		18	1.7	Y	5	80
1	H	3	30	3	0.03793	18.7			16		24.1	2	Y	5	80
2	H	2	60	5.26	0.04077	13.7			13.6		31.2	1.1	Y	10	80
2	H	4	80	8.46	0.007553	22.9			24.9		22.6	5.2	Y	10	80
2	H	6	30	10.96	0.003885	16.3			15.4		14.5	6.6	Y	10	80
3	H	2	80	15.1	0.00448	21.8	34.6	355.6	17.2	355.8	26.8	7.9	Y	10	40
3	H	4	100	18.24	0.003956	17.1	14.2	335.2	25.8	334.7	18.8	10.3	Y	5	80
3	H	6	75	20.92	0.0008873	14.6	18.4	339.4	26.4	334.5	21.3	10.1	Y	5	80
4	H	2	50	24.3	0.001176	10.2	338.2	336.2	10.7	332.9	18.4	8.7	Y	10	80
4	H	4	60	27.4											
4	H	6	65	30.45	0.00264	20.6	316.3	314.3							
5	H	2	80	34.1	0.0006773	16.1	273.8	323.8							
5	H	4	86	37.09											
5	H	6	75	39.91	0.0009099	5.9	265.7	315.7							
6	H	2	38	43.18	0.001106	24.6	75.7	349.7	26.1	348.4	39.8	6.4	Y	10	80
6	H	4	80	46.57											
6	H	6	40	49.12		5.3	62.1	336.1							
7	H	2	40	52.7		14.7	289	311							
7	H	4	80	56.1											
7	H	6	75	59.05	0.001127	17.8	288.6	310.6	13.2	308.6	35.8	6.6	Y	10	80
8	H	2	88	62.68	0.000951	10.3	162.9	333.9	7.7	331.8	28.8	4.9	Y	10	80
8	H	4	60	65.4											
8	H	6	50	68.3		23.1	165.7	336.7							
9	H	2	75	72.05	0.001127	11.5	184.4	346.4	16.6	348.4	24.4	10.6	Y	5	80
9	H	4	56	74.86											
9	H	6	60	77.9	0.001268	10.5	176.3	338.3	20.8	343.6	41.8	9.9	Y	5	60
10	H	2	40	81.21	0.0007459	10.6	141.7	306.7	17.5	305	20.5	10.4	Y	5	40
10	H	4	120	85.1											
10	H	6	80	87.78	0.001602	28.1	140.3	305.3	34.3	309.3	31.6	7.5	Y	5	60
11	H	2	80	91.02		19.4	28.1	329.1							
11	H	4	111	94.17											
11	H	6	80	96.82		28.2	18.2	319.2							
12	H	2	72	100.44		3.5	177.4	335.4							
12	H	4	70	103.26		13.4	155	313							
12	H	6	75	106.14		30.7	211.2	9.2							
13	H	3	50	111.09		17.5	180.2	329.2							
13	H	5	56	112.73		8.2	140.4	289.4							
13	H	6	80	114.39		26.4	140.2	289.2							
14	H	2	75	118.67		−6.1	201.9	308.9							
14	H	4	70	121.5		20.2	154.3	261.3							
14	H	6	50	124.28		3.8	190.8	297.8							
15	H	2	60	128.02		−22	108.3	206.3							
15	H	4	95	131.21		8.8	145.9	243.9							
15	H	6	55	133.65		34.2	89.2	187.2							
16	H	2	70	137.68		8.4	223.7	282.7							
16	H	4	100	140.85		52.6	210.8	269.8							
16	H	6	40	143.21		38.9	72.9	131.9							
17	H	2	60	147.02		15.3	116.2	247.2							
17	H	4	80	150.03		6.5	119.1	250.1							
17	H	5	110	151.79		34.7	80.4	211.4							
18	H	2	50	156.27		46.4	191.7	153.7							
18	H	4	33	158.63	0.0006401	−12.4	162.1	124.1	−12.2	121.8	9.2	8.2	Y	10	30
18	H	6	80	161.99		−5.2	182.6	144.6							
19	H	2	98	166.4		21.3	173.7	35.6							
19	H	5	75	170.47		−2.8	257.7	119.6							
20	H	3	75	176.31		3.7	258.7	350.2							
20	H	7	50	181.89		−28.3	148.1	239.6							
21	H	2	40	184.82		23.1	107.6	273.7							
21	H	6	45	190.02		19.1	278.3	84.4							
22	H	1	90	193.4		4	150.2	86.6							
22	H	2	58	194.5		16	195.2	131.6							
22	H	4	90	197.65		17.1	138.9	75.3							
23	H	4	99	206.85		29.7	347.2	151.1							
23	H	5	89	208.16		11.3	108.8	272.7							
23	H	6	28	208.96		56	16.2	180.1							

Table T12 (continued). (Continued on next page.)

Core	Type	Section	Top offset (cm)	Top depth CSF-A (m)	NRM (A/m)	Inclination (AF 10 mT) (°)	Declination (AF 10 mT) (°)	True declination (AF 10 mT) (°)	PCA inclination (°)	True PCA declination (°)	PCA MAD1 (°)	PCA MAD3 (°)	PCA anchored	PCA start (mT)	PCA end (mT)
24	H	3	65	214.96		32.8	220.9	135.7							
24	H	6	55	219.19		20.1	118.6	33.4							
24	H	7	52	220.62		34.4	148.2	63							
25	H	3	98	224.86		38.8	250.7	331.8							
25	H	5	63	227.38		49.4	134.4	215.5							
25	H	6	93	229.15		34.2	175.1	256.2							
26	H	2	80	232.71	0.0009976	10	199.9	338.3	14.9	338.5	9.4	6.7	Y	5	30
26	H	4	62	235.35		19.7	149.2	287.6							
26	H	6	46	238.05	0.001276	13.4	196.8	335.2	13.8	333.9	10.2	3.1	Y	10	40
27	H	2	84	242.24	0.0009596	15.1	265.3	14.6	28.5	8.7	4.8	15.9	Y	5	30
27	H	4	34	244.54											
28	H	2	79	251.68	0.0007232	9.9	117.9	227.2	8.7	295.7	24.4	3.2	Y	10	40
28	H	4	9	253.79											
29	H	2	57	256.87	0.0009297	18.9	247.2	350.3	39.9	347.9	18.8	10.3	Y	5	30
29	H	4	62	259.78		18.8	217.5	320.6		103.1					
30	F	2	59	262.99											
31	F	1	76	266.56											
32	F	1	43	271.03											
32	F	3	39	273.51											
33	F	3	47	278.69											
34	F	2	38	280.86											
35	F	2	88	287.24											
35	F	4	40	289.73											
36	F	1	65	290.45											
36	F	3	69	293.17											
37	F	1	73	295.33											
37	F	3	75	298.1											
38	F	2	34	301.23											
39	F	2	53	306.12											
39	F	4	36	308.81											
40	F	2	42	310.86											
40	F	4	52	313.48											
42	F	2	30	316.32											
42	F	4	56	318.87	0.003243				45		7.4	11.9	Y	5	30
43	F	2	70	322.04	0.003193				59.1		5.1	19.3	Y	5	30
43	F	3	80	323.68											
44	F	3	40	326.99	0.002072				58.2		11.8	13.7	Y	5	40
45	X	2	46	330.76											
45	X	3	59	332.39											
47	X	2	90	344.57	0.001079				46.3		13.6	8.8	Y	5	40
47	X	4	95	347.64											
47	X	6	85	350.56											
48	X	2	83	354.05	0.004715				27		5.9	9.2	Y	20	40
48	X	4	84	357.06											
48	X	6	73	359.87											
49	X	2	59	364.3											
49	X	4	64	367.36											
49	X	6	58	370.3											
50	X	2	106	374.46	0.002337				63.6		11.5	5.4	Y	10	30
50	X	4	96	377.36											
50	X	6	52	379.92	0.002363				55.4		15.2	4.8	Y	5	30
51	X	2	51	383.61	0.001828				41.5		12.8	13.9	Y	10	30
51	X	4	95	387.02											
51	X	6	60	389.67	0.00113				68.3		17.4	4.5	Y	5	30
52	X	2	87	392.54											
52	X	4	69	395.36											
52	X	6	89	398.56											
53	X	2	92	403.42											
53	X	4	58	405.99											
53	X	6	73	409.14											
54	X	2	85	413.05	0.001498				67.9		31	5.7	Y	5	30
54	X	4	85	416.05											
54	X	6	65	418.85											
55	X	2	69	422.59											
55	X	4	101	425.93											
55	X	6	70	428.64											
56	X	2	93	432.53											

Table T12 (continued).

Core	Type	Section	Top offset (cm)	Top depth CSF-A (m)	NRM (A/m)	Inclination (AF 10 mT) (°)	Declination (AF 10 mT) (°)	True declination (AF 10 mT) (°)	PCA inclination (°)	True PCA declination (°)	PCA MAD1 (°)	PCA MAD3 (°)	PCA anchored	PCA start (mT)	PCA end (mT)
56	X	4	63	435.23											
56	X	6	71	438.31											
57	X	4	44	444.74	0.001932				–43.4		14.9	7.4	Y	10	40
57	X	6	42	447.72											
58	X	2	62	451.62	0.00227				43.2		4.3	16.5	Y	5	40
58	X	4	53	454.53											
59	X	2	97	460.87											
59	X	6	60	466.5											
60	X	2	80	471.2											
60	X	6	30	476.7											
61	X	2	28	480.38											
61	X	6	45	486.55											
62	X	2	61	490.41											
62	X	6	54	496.34											
63	X	2	35	499.85											
63	X	4	46	502.96	0.002587				37.9		9.5	11.1	Y	10	30
64	X	2	96	510.16	0.001299				44.1		21.9	11.3	Y	15	30
64	X	4	117	513.37	0.00175				41.5		18.3	5.3	Y	10	40
65	X	2	76	519.66	0.001333				47		20	12.9	Y	10	30
65	X	4	60	522.5	0.001483				52.9		27.2	6.9	Y	5	20
66	X	2	96	528.36											
66	X	4	102	531.42											
66	X	6	81	534.05											
67	X	2	82	539.12	0.001335				32.9		38.8	7.2	Y	15	30
67	X	4	102	542.32											
67	X	6	62	544.92	0.002498				37		9.5	6	Y	15	30
68	X	2	34	547.12											
68	X	6	83	553.25											
69	X	2	49	558.2											
69	X	6	50	564.1											
71	X	2	85	576.82											
71	X	6	74	582.54											
72	X	2	50	587.3											
72	X	6	67	593.51											
73	X	2	67	597.17											
73	X	6	65	603.16											
74	X	2	111	607.31											
74	X	5	40	611.13											
75	X	2	94	616.84											
75	X	6	43	622.33											
76	X	2	55	626.15	0.002705				38.6		13.7	7.5	Y	10	80
76	X	4	50	629.1											
76	X	5	78	630.88											
77	X	2	50	635.8	0.002949				5		1.7	3.9	Y	40	80
77	X	4	82	639.08											
77	X	6	42	640.91											
78	X	2	82	645.82	0.02439				41.1		21.5	2.7	Y	20	80
78	X	3	55	647.05											
79	X	2	75	649.96	0.002491				47		25	8.4	Y	20	80
79	X	4	50	652.71											
80	X	2	80	655.6											
80	X	4	97	658.77	0.003218				53		17.4	4.6	Y	20	80
81	X	1	29	663.29											
81	X	3	72	666.72											
81	X	6	72	671.22											

(Sample 353-U1447A-10H-6W, 80–82 cm [87.78 m CSF-A]), but PCA did not work well for deeper samples. Most of the natural remanent magnetization was lost during the first few demagnetization steps (up to 10–15 mT), with a significant drilling-related vertical overprint (Figure **F19**). Cores 353-U1447A-26H through 28H (230.5–254.88 m CSF-A) revealed a clear remanence pattern from both archive halves (Figure **F17**) and discrete samples. Both measurements indicate positive (normal) polarity for these depth ranges. For HLAPC and XCB cores, large drilling overprints prevent any determination of magnetostratigraphy.

Although many discrete samples did not show good results from PCA, we observe that the remanence direction during AF demagne-

Table T13. Summary of core orientation picks, Site U1447. MTF = magnetic toolface. **Download table in .csv format.**

Core	Hole U1447A MTF	Hole U1447A Range	Hole U1447C MTF
1H	—		
2H	—		
3H	321.0		
4H	358.0		221.5
5H	104.0	50–141	196.6
6H	274.0		206.6
7H	22.0		221.0
8H	171.0		283.0
9H	162.0		200.4
10H	172.0	165–180	227.3
11H	301.0	296–306	143.4
12H	158.0		149.4
13H	149.0		198.2
14H	107.0		69.5
15H	75.0	55–98	200.1
16H	59.0		206.6
17H	131.0		
18H	322.0		
19H	221.9		
20H	91.5		
21H	166.1		
22H	296.4		
23H	163.9		
24H	274.8		
25H	81.1		
26H	138.4		
27H	109.3		
28H	180.0		
29H	103.1		

tization often concentrates around a single point for each sample (after the first few steps of demagnetization) before the direction becomes scattered at high AF steps (Figure **F19B**). In addition, the remanence measured on samples from the same APC core often migrates toward a common direction. To investigate the significance of this direction, we plotted the depth variation in the remanence directions of discrete samples after 10 mT demagnetization (Figure **F20**). The declination data concentrate around 0° (360°) shallower than Sample 353-U1447A-13H-3W, 50–52 cm (119.09 m CSF-A), close to 180° deeper than Sample 16H-4W, 100–102 cm (137.68 m CSF-A), and back to 0° (360°) deeper than Sample 26H-2W, 80–82 cm (232.71 m CSF-A). As expected, this pattern is similar to trends in section measurements, albeit with less scatter. Note that the reliability of these declinations in determining a magnetostratigraphy is debatable because stepwise AF demagnetization shows variable ChRM stability within discrete samples.

We construct two classes of magnetostratigraphy for Site U1447 using two sets of data with different reliability (Table **T14**). The first (Class 1) utilizes archive-half measurements and PCA directions of discrete samples, whereas the second (Class 2) uses inclination and declination from discrete samples after 10 mT demagnetization to the same interval where the Class 1 magnetostratigraphy was inconclusive (Figure **F20**). Class 1 should be considered as more conservative, as it is based on the same methodology used at other sites during Expedition 353.

Figure F19. A–B. Representative stepwise AF demagnetization results, Hole U1447A discrete samples. For the orthogonal vector plot, red symbols = points used in PCA, and blue lines = calculated ChRM direction.

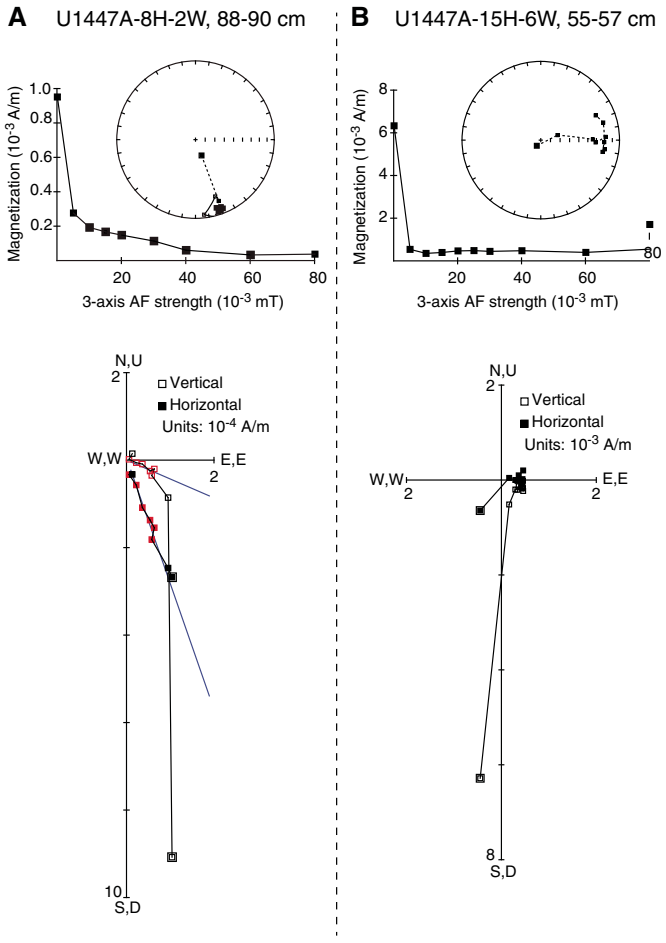

Bulk magnetic properties

ARM (0.05 mT direct current field, 80 mT AF) was acquired on a selection of discrete samples taken from the working halves of Hole U1447A. ARM broadly measures relative changes in the concentration of ferrimagnetic minerals, where increases in the concentration of finer grained particles will increase ARM values much greater than an equivalent change in coarser grained particles. A significant decrease in ARM values for Hole U1447A at 10 m CSF-A (Figure **F21**) suggests either a decrease in the input, or the removal, of fine-grained ferrimagnetic minerals. A similar decrease is observed in magnetic susceptibility (see **Physical properties**) and is likely a response to early diagenesis (see **Geochemistry**). The decrease in ARM values at this depth (10 m CSF-A) is similar to what we see at IODP Site U1445 in the Mahanadi basin (see **Paleomagnetism** in the Site U1445 chapter [Clemens et al., 2016c]). From 10 to 240 m CSF-A, ARM is fairly stable and then it begins to increase to a peak value at 310 m CSF-A, approximately coinciding with lithostratigraphic Unit III. The increased and less stable ARM values deeper than 240 m CSF-A may be related to a lack of biosilica (see **Lithostratigraphy**) that could be diluting the magnetic record.

Figure F20. A. Class 1 depth variations of PCA declination and inclination from discrete samples compared with section data for Hole U1447A. B. Class 2 depth variations in declination and inclination from discrete samples after 10 mT AF demagnetization. Magnetostratigraphy is also shown based on both classes.

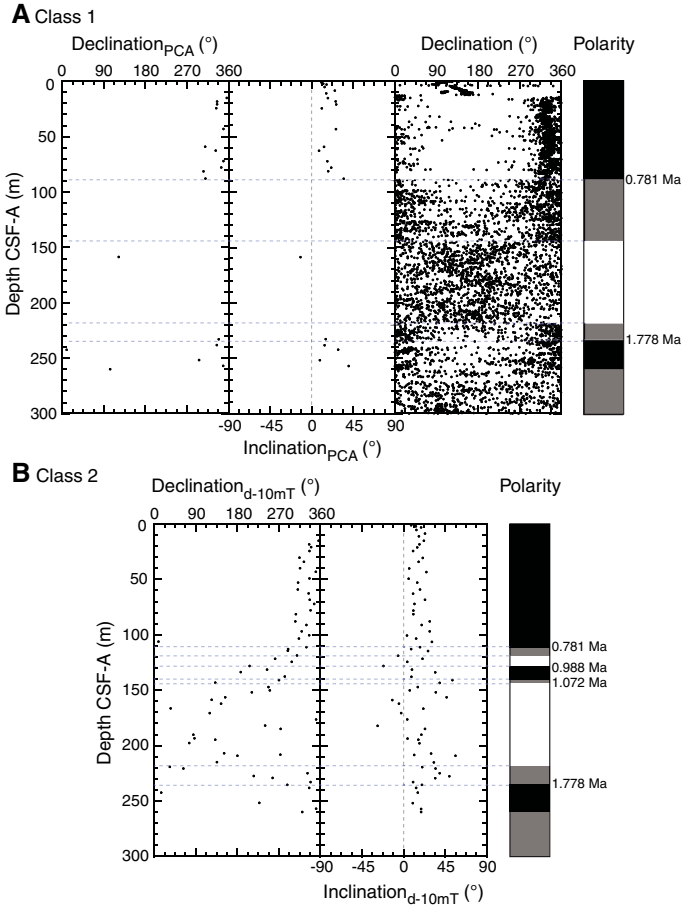

Table T14. Summary of magnetostratigraphy, Site U1447. Class 1 represents more conservative estimates than Class 2. See text for discussion. **Download table in .csv format.**

Class 1 chron top depth CSF-A (m)	Class 2 chron top depth CSF-A (m)	Chron top age (Ma)	Chron name
0	0	0	C1n (Brunhes)
89–145	111.1–118.7	0.781	C1r.1r (Matuyama)
NA	128–140	0.988	C1r.1n (Jaramillo)
NA	143–145	1.072	C1r.2r
218.5–234.5	218.5–234.5	1.778	C1r.2n (Olduvai)

Figure F21. Depth variation in mass-normalized ARM, Hole U1447A. Dashed gray lines = lithostratigraphic unit boundaries.

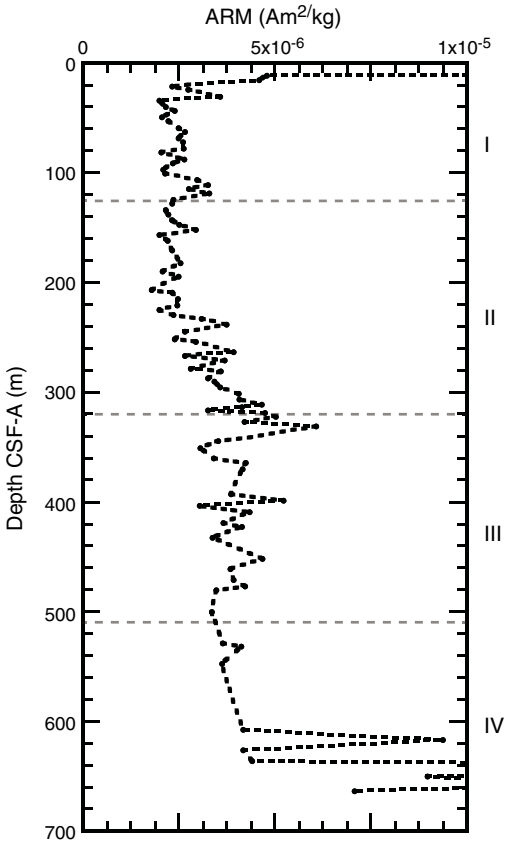

Physical properties

Standard physical property measurements were collected at Site U1447 with the addition of thermal infrared (IR) scanning of cores on the catwalk for the detection of temperature anomalies that could possibly be related to gas hydrate. Data from Hole U1447B are presented but are not discussed, as the hole was dedicated to high-resolution geochemistry. Overall, we were able to identify four physical property (PP) units based on significant changes with the physical property data sets: Units 1 (0–200 m CSF-A), 2 (200–320 m CSF-A), 3 (320–570 m CSF-A), and 4 (570–730 m CSF-A) (Table **T15**). In general, data from both Holes U1447A and U1447C are in good agreement.

Gamma ray attenuation (GRA), MS, *P*-wave velocity (V_P), and NGR measurements were acquired on all whole-round sections using the Special Task Multisensor Logger (STMSL), the Whole-Round Multisensor Logger (WRMSL), and the Natural Gamma Ra-

diation Logger (NGRL). Whole-round sections from Hole U1447A were logged on the STMSL (5 cm resolution) and WRMSL (at 5 cm resolution) before being taken to the core rack for thermal equilibration (~19°C). For Hole U1447C, alternate sections were run on the STMSL (Sections 1, 3, 5, and 7) and WRMSL (Sections 2, 4, 6, 8, and CC). We measured alternate sections in Hole U1447C to maximize logging efficiency in order to assist the stratigraphic correlation process. The *P*-wave logger (PWL) produced unreliable data; therefore, it was disabled for the remainder of Hole U1447C. Following thermal equilibration, sections were logged on the NGRL. Approximately 10 cm^3 sediment samples were collected from the working halves of Sections 2, 4, and 6 from Hole U1447A for moisture and density (MAD) analyses. The archive-half sections were used to collect color reflectance and point MS data on the Section Half Multisensor Logger (SHMSL) and red, green, and blue (RGB) data on the Section Half Imaging Logger (SHIL). The data presented in this report were conditioned to remove outliers related to endcaps, voids, and foam spacers (see **Physical properties** in the Expedition 353 methods chapter [Clemens et al., 2016a]). We summarize statistics (minimum, maximum, and mean) of all measured parameters downhole for Holes U1447A–U1447C for comparison (Table **T16**).

Table T15. Physical property units, Site U1447. **Download table in .csv format.**

Unit	Depth CSF-A (m)
1	0–200
2	200–320
3	320–570
4	570–730

Table T16. Minimum, maximum, and mean statistics of measured physical property data, Holes U1447A–U1447C. MAD = moisture and density, SHMSL = Section Half Multisensor Logger, MS = magnetic susceptibility, NGR = natural gamma radiation, STMSL = Special Task Multisensor Logger, WRMSL = Whole-Round Multisensor Logger. **Download table in .csv format.**

Attribute	Minimum	Maximum	Mean
Hole U1447A			
L*	28	56.8	40.08
a*	–2.9	2.8	–0.17
b*	–6	9.9	1.58
Red	26.1	74.8	47.37
Green	25.4	75	46.96
Blue	21.7	71	41.78
MAD density (g/cm^3)	1.35	1.89	1.73
STMSL density (g/cm^3)	1.1	1.96	1.68
WRMSL density (g/cm^3)	1.01	1.97	1.7
MAD porosity (%)	49.9	80.8	58.84
SHMSL MS (IU)	–0.67	60	13.88
STMSL MS (IU)	0	100	11.03
WRMSL MS (IU)	1	88.67	9.97
NGR (counts/s)	6.49	57.57	32.13
Hole U1447B			
L*	18.9	47.6	37.77
a*	–1.5	1.9	–0.33
b*	–0.3	8.8	3.66
Red	14	61.4	46.31
Green	13.5	57.5	44.72
Blue	13.5	49.9	37.88
STMSL density (g/cm^3)	1.1	1.56	1.44
WRMSL density (g/cm^3)	1.21	1.89	1.47
SHMSL MS (IU)	14.67	49.33	25.69
STMSL MS (IU)	1.28	22.65	10.77
WRMSL MS (IU)	2	18	9.02
NGR (counts/s)	14.49	29.98	23.87
Hole U1447C			
L*	29.6	50.8	38.68
a*	–1.6	2.9	0.18
b*	–2.1	8.6	1.5
Red	9.5	64.6	46.35
Green	9	63.4	45.18
Blue	8.9	59.5	39.34
STMSL density (g/cm^3)	1.12	1.89	1.59
WRMSL density (g/cm^3)	1.34	1.89	1.62
SHMSL MS (IU)	5	44	18.88
STMSL MS (IU)	4.27	23.08	9.54
WRMSL MS (IU)	1.33	21	9
NGR (counts/s)	15.22	39.08	31.04

Magnetic susceptibility

STMSL and WRMSL MS values recorded for Hole U1447A vary between 1.0 and 50 instrument units (IU) (Figure **F22**; Table **T16**). Occasional values >50 IU were recorded in PP Unit 4. The top of PP Unit 1 (0–200 m CSF-A) is characterized by moderate variability in the upper ~150 m CSF-A, which then decreases to the end of the unit boundary (Figure **F22**). In PP Unit 2, MS values increase steadily downhole to the boundary of PP Unit 3, where MS variability is fairly steady to ~500 m CSF-A. Deeper than ~500 m CSF-A, MS decreases with small fluctuations. MS values increase around 650 m CSF-A and again at the end of the hole. The STMSL and WRMSL track measurements agree well, but the SHMSL point measurements are significantly offset to higher values deeper than 490 m CSF-A; however, the overall trend is similar to the whole-round variability in Hole U1447A. Hole U1447B was a short geochemistry hole (Figure **F23**) and its physical property data are not being discussed here. The downhole trend and cyclicity in MS in Hole U1447C broadly agrees with Hole U1447A (Figures **F22**, **F24**).

Figure F22. Physical properties showing downhole variability in magnetic susceptibility from WRMSL, STMSL, and point SHMSL; density from WRMSL, STMSL, and MAD (red points); porosity; and NGR, Hole U1447A.

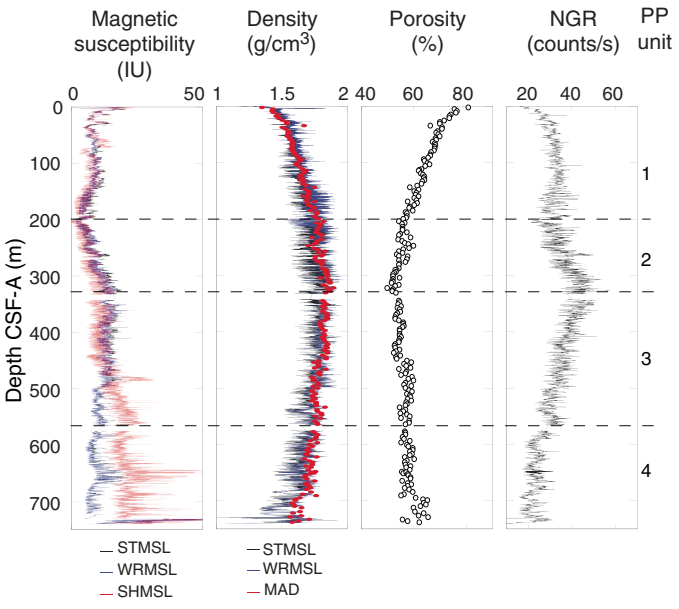

Figure F23. Physical properties showing downhole variability in magnetic susceptibility from WRMSL, STMSL, and point SHMSL; density from WRMSL and STMSL; and NGR, Hole U1447B.

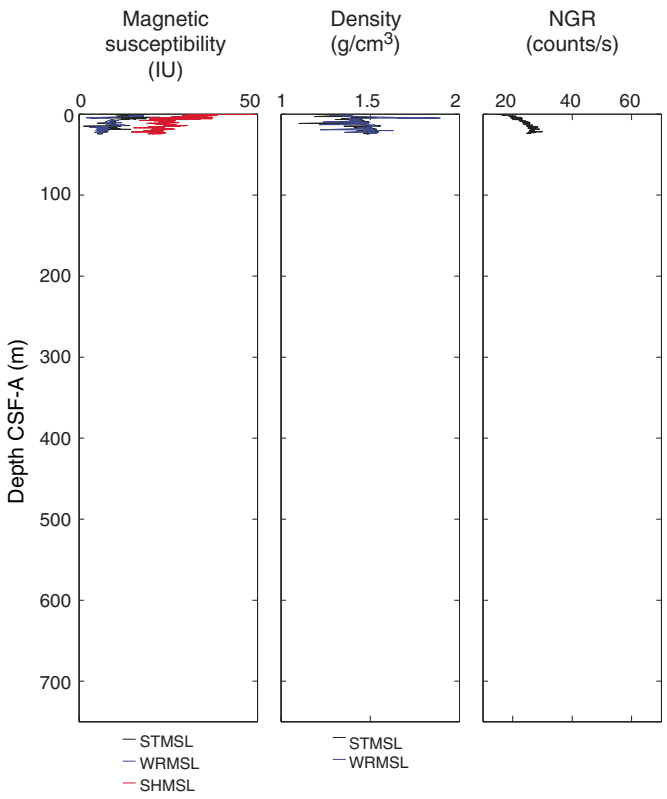

Figure F24. Physical properties showing downhole variability in magnetic susceptibility from WRMSL, STMSL, and point SHMSL; density from WRMSL and STMSL; and NGR, Hole U1447C.

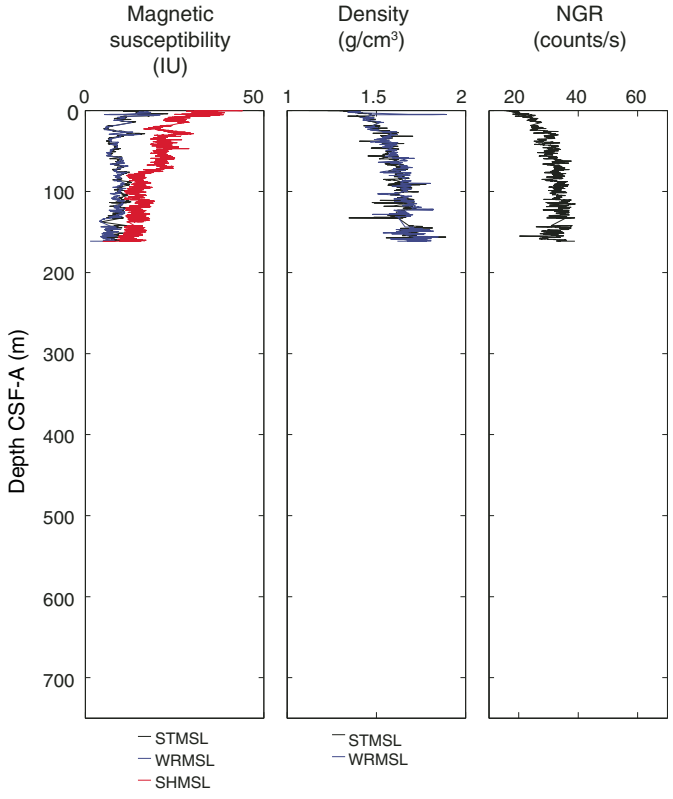

Natural gamma radiation

NGR counts range from ~6.49 to 57.57 counts/s with an average of 32.13 counts/s in Hole U1447A and from 15.22 to 39.08 counts/s with an average of 31.04 counts/s in Hole U1447C. NGR data show long-term cyclic variability downhole, possibly related to changes in continental input or clay concentrations (Figure **F22**; see **Lithostratigraphy**). The downhole trend and cyclicity in NGR counts in Hole U1447C broadly agrees with Hole U1447A (Figures **F22**, **F24**).

GRA and MAD bulk density

The bulk density at Site U1447 was measured using (1) the GRA method using the STMSL and WRMSL that provides bulk density estimates from whole-round sections from Holes U1447A–U1447C (Figures **F22**, **F23**, **F24**) and (2) MAD measurements on discrete samples that provide a second, independent measure of bulk density and the dry density, grain density, water content, and porosity from Hole U1447A only (Figure **F22**). The density data from MAD and GRA show good agreement, and the overall trend in GRA data between Holes U1447A and U1447C are in good agreement.

For Hole U1447A, the GRA bulk density values range from ~1 to 1.96 g/cm^3, whereas MAD bulk density ranges between 1.35 and 1.89 g/cm^3 in Hole U1447A. The mean MAD bulk density is 1.71 g/cm^3 (bulk) and 1.09 g/cm^3 (grain) with a minimum dry density of 0.61 g/cm^3 and a maximum dry density of 1.54 g/cm^3. The porosity values vary significantly downhole and range between 44.1% and 77.3% (Figure **F22**).

Generally, density increases with a corresponding decrease in porosity with depth, mainly due to sediment compaction (e.g., until PP Unit 2). We observe a general decrease in MAD density and a corresponding increase in porosity, indicating changes in sediment composition, in PP Units 3 and 4 (see **Lithostratigraphy**). A gap in coring occurred at ~570 m CSF-A, at the bottom of the PP Unit 3. Both Holes U1447A and U1447C whole-round density data agree downhole.

Compressional wave velocity

No *P*-wave velocity measurements using the PWL were collected due to the instrument malfunctioning.

Diffuse reflectance spectroscopy and digital color image

Spectral reflectance was measured on all archive halves using the SHMSL. There are slight color variations downhole in Holes U1447A, U1447B, and U1447C (Figures **F25**, **F26**, **F27**). L* values range between 28 and 56.8 with an average value of 40.08 (Table **T16**). Reflectance a* and b* values range between −0.6 and 9.9 (average = −0.17) and between −6 and 9.9 (average = 1.58), in Holes U1447A and U1447C, respectively. The reflectance b* trend decreases in PP Unit 1 and then increases until end of the Unit 1 boundary. In PP Unit 2, b* decreases and then increases again in PP Unit 3 and continues to increase until ~730 m CSF-A (Figures **F25**, **F26**, **F27**).

The SHIL data (RGB) were recorded from the surface of the split archive halves prior to drying. The raw RGB data averages are R = 47.37, G = 46.96, and B = 41.78 in Hole U1447A (Figure **F28**). Hole U1447B and U1447C RGB data are shown in Figures **F29** and **F30**.

Figure F25. L*, a*, and b* data, Hole U1447A.

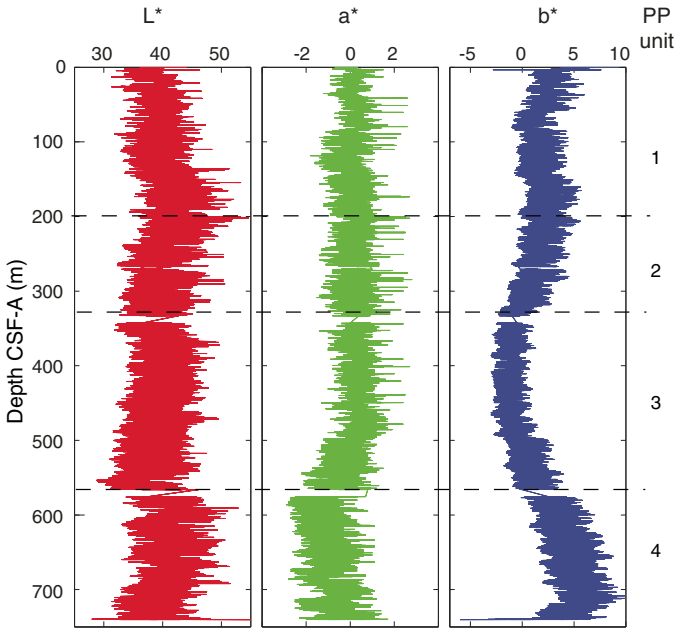

Figure F26. L*, a*, and b* data, Hole U1447B.

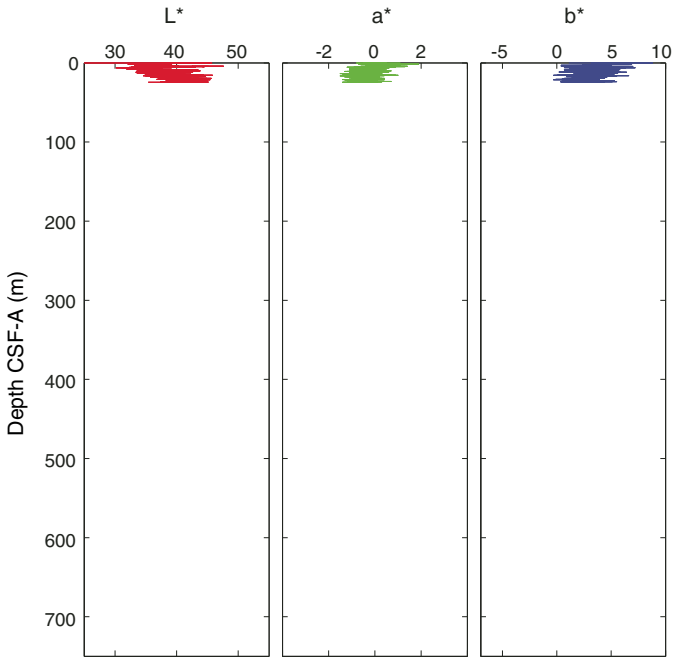

Figure F27. L*, a*, and b* data, Hole U1447C.

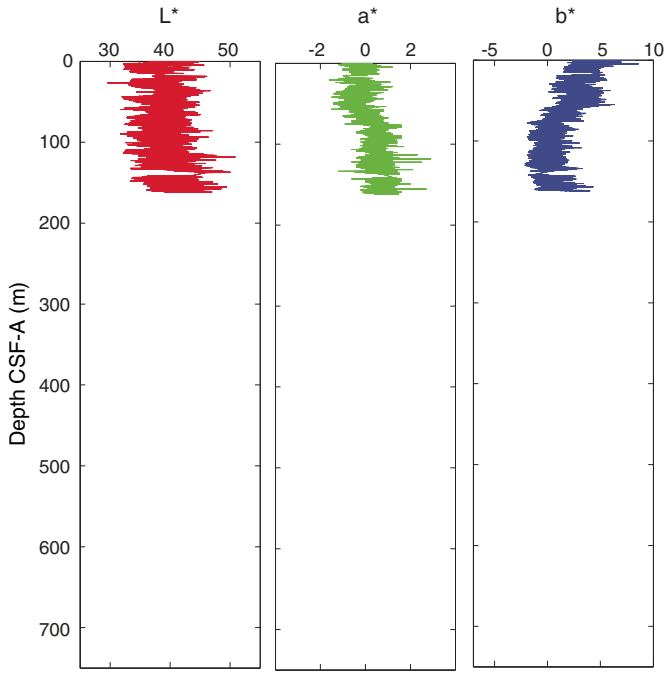

Figure F28. SHIL RGB color data, Hole U1447A.

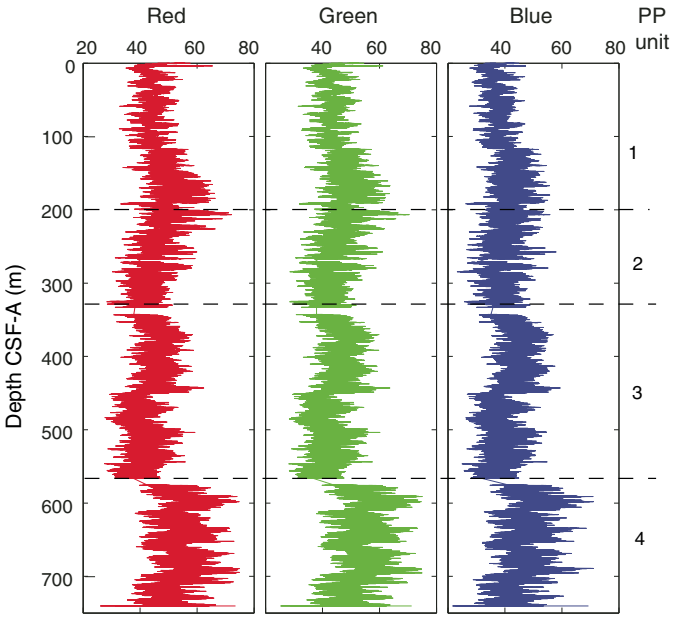

We summarize variability in RGB statistics (minimum, maximum, and mean) in Table **T16**.

Downhole temperature

Standard downhole temperature measurements were made at the sediment/water interface and then on Cores 353-U1447A-4H, 7H, 10H, and 15H using the APCT-3 (Table **T17**). Using the depth-related temperature change, the geothermal gradient is ~27.3°C/km (Figure **F31**).

Thermal infrared temperature

A FLIR thermal IR camera was used for thermal imaging of cores upon arrival to the catwalk. No clear IR anomalies were found.

Summary

Based on the overall trends within individual physical property data sets, we divided Hole U1447A into four units. The changes in bulk density and porosity reflect changes in sediment composition.

Figure F29. SHIL RGB color data, Hole U1447B.

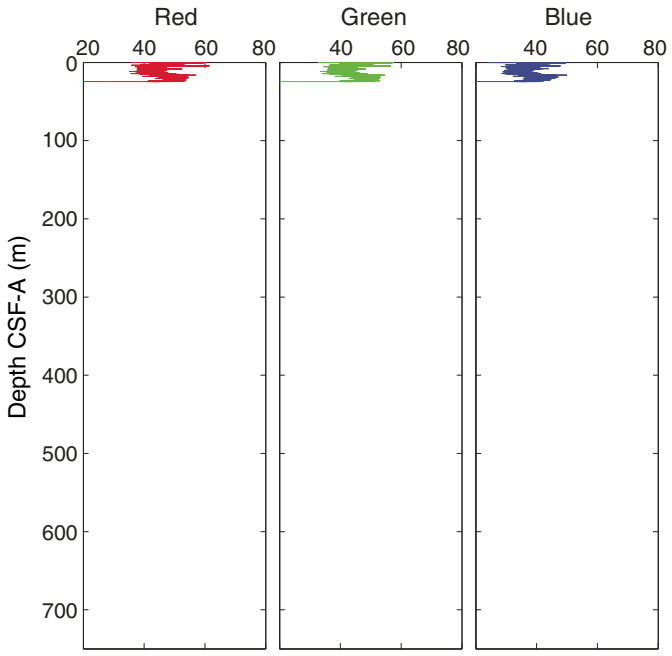

Figure F30. SHIL RGB color data, Hole U1447C.

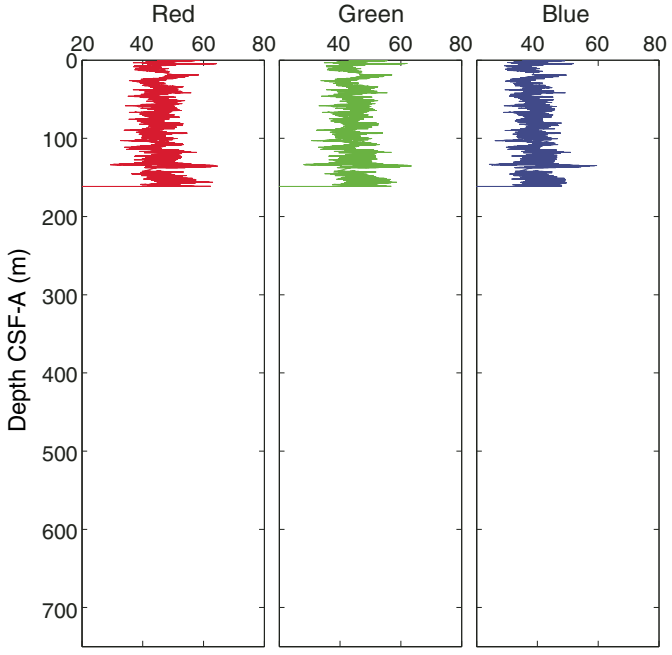

Table T17. Downhole temperature data from the APCT-3, Hole U1447A. **Download table in .csv format.**

Depth CSF-A (m)	Temperature (°C)
0	5.1
31.79	6.11
60.27	7.05
89.12	7.53
135.68	8.66

Figure F31. Downhole temperature data, Hole U1447A.

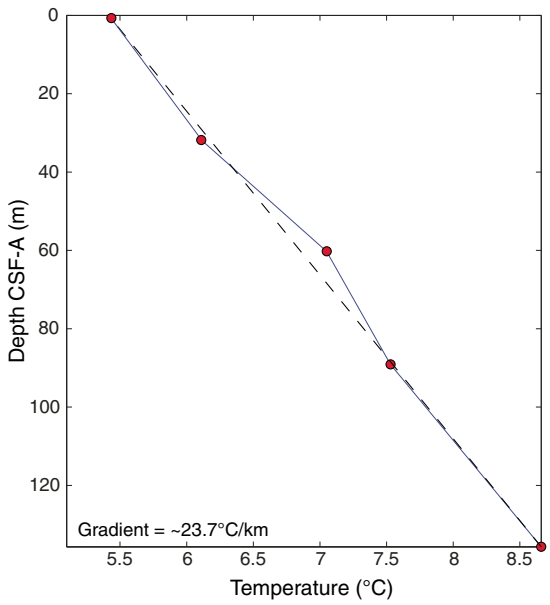

We observe similar trends in all physical property data between Holes U1447A and U1447C. Long-term cyclic variability in NGR values may reflect periodic changes in lithogenic input.

Stratigraphic correlation

A composite scale (CCSF-A) and a splice (CCSF-D) were constructed for Site U1447 using Holes U1447A and U1447C (as defined in **Stratigraphic correlation** in the Expedition 353 methods chapter [Clemens et al., 2016a]). Splicing among these holes enabled us to construct a continuous stratigraphic sequence to ~147 m CCSF-D (Tables **T18**, **T19**; Figure **F32**). Hole U1447B, dedicated to geochemical sampling on board the ship, was short and not used in splicing; however, we tied it to the same composite scale as Holes U1447A and U1447C.

Construction of CCSF-A scale

We selected the core with the best mudline recovery (Core 353-U1447C-1H) to anchor the composite depth scale and defined the top as 0 m CCSF-A. The CCSF-A scale for Site U1447 (see Table **T18**) is based on correlation of RGB color data and secondarily on MS and on NGR data. RGB green was utilized in correlations for Site U1447. MS and NGR were measured on whole-round sections, whereas RGB was measured on archive-half sections (see **Physical properties** for details). The R, G, and B components of the RGB triplet are highly correlated to each other because, on the first order, all are measures of the reflectivity of the sediment. The small differences between R, G, and B can be expressed as ratios such as red/green, red/blue, or green/blue. However, ratios were not employed in our correlation due to lack of time (see the **Expedition 353 methods** chapter [Clemens et al., 2016a]). Reflectance spectroscopy data (i.e., L*, a*, and b*), which can produce information similar to RGB ratios, were not used for correlation due to inconsistent variability from hole to hole resulting from low-quality wavelength spectra collected by the Ocean Optics USB4000 spectrophotometer on the monotonously dark sediments of Site U1447.

Table T18. Vertical offsets applied to cores in order to align structure in adjacent holes, Site U1447. **Download table in .csv format.**

Table T19. Splice intervals, Site U1447. **Download table in .csv format.**

Figure F32. Core alignment shown using (A) RGB blue (used in lieu of green due to availability of outlier-cleaned data), (B) NGR, and (C) MS profiles, Holes U1447A–U1447C. Spliced profile is also shown. Splice tie points are indicated by black vertical lines. Original KaleidaGraph files are available in STRATCOR in **Supplementary material**.

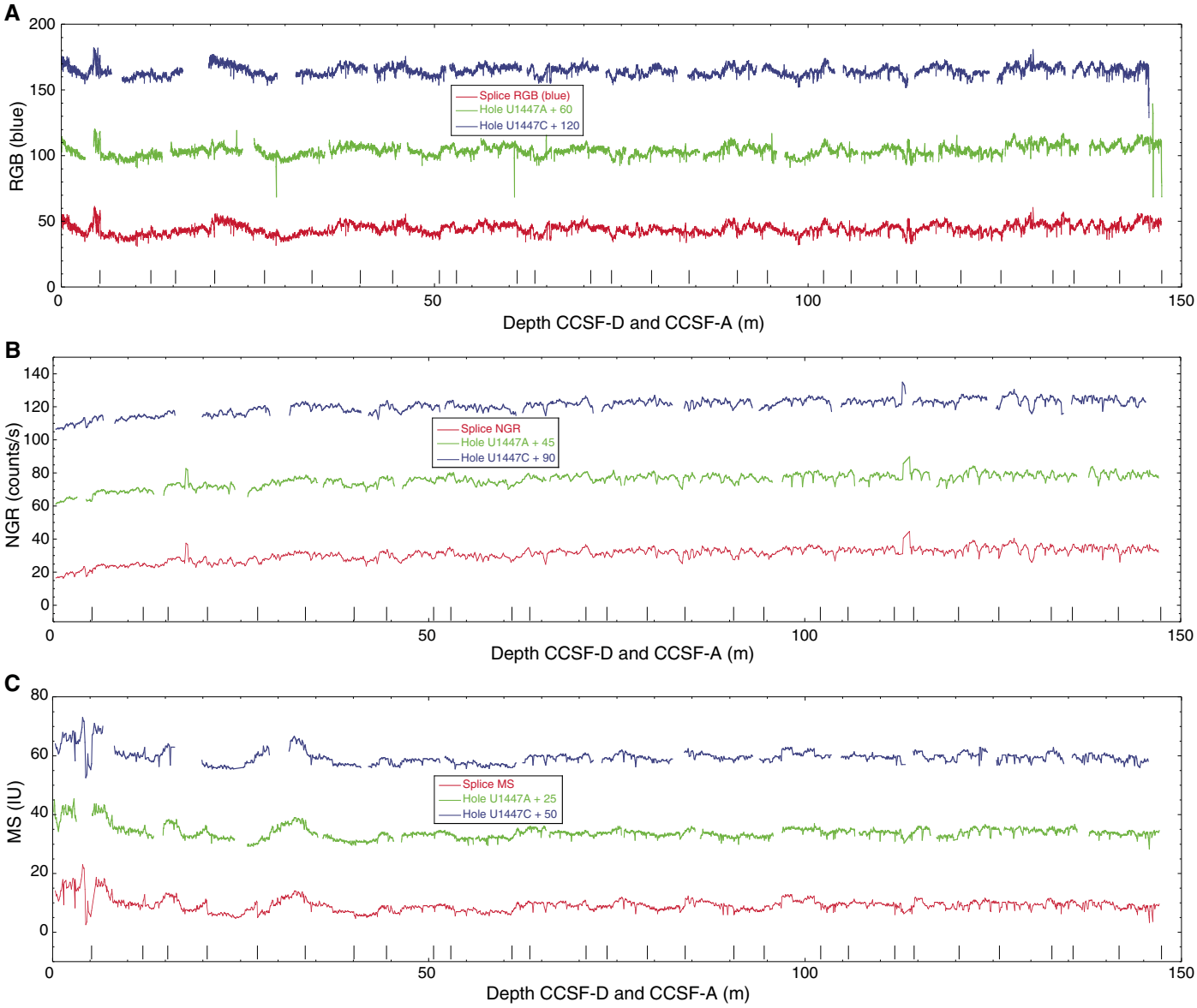

Construction of CCSF-D scale

A combination of Holes U1447A and U1447C cover the stratigraphic section to ~147 m CCSF-D. When constructing the splice, we tried to minimize inclusion of disturbed intervals and avoid whole-round sampling intervals (notably from Hole U1447A) as much as possible. Selected splice intervals are listed in Table **T19**. Postcruise, the splice interval tables were modified using the Splice-File-Fixer program to ensure that each depth has been assigned the correct sample ID. Both the affine and the corrected splice interval tables were uploaded into Laboratory Information Management System (LIMS) during the first postcruise meeting in June 2015. The core top depths in the affine tables were not corrected and hence may be slightly incorrect in a range of <2 cm. However, the offsets are correct.

Reliance on RGB, which sometimes has a fuzzy character due to cracks and defects of the split core surface, precluded, in places, the definition of unique correlation features and general trends were used instead, reducing the accuracy of the splice to the decimeter range. As a result, correlation should be viewed with caution deeper than ~112 m CCSF-A, notably if high-resolution sampling is planned. Onshore X-ray fluorescence scanning, color reflectance rescanning, and bulk $\delta^{18}O$ should provide better means of correlation.

References

Awasthi, N., Ray, J.S., Singh, A.K., Band, S.T., and Rai, V.K., 2014. Provenance of the late Quaternary sediments in the Andaman Sea: implications for monsoon variability and ocean circulation. *Geochemistry, Geophysics, Geosystems,* 15(10):3890–3906. **http://dx.doi.org/10.1002/2014GC005462**

Barron, J.A., 1985. Miocene to Holocene planktic diatoms. *In* Bolli, H.M., Saunders, J.B., and Perch-Nielsen, K. (Eds.), *Plankton Stratigraphy:* Cambridge, United Kingdom (Cambridge University Press), 763–809.

Bown, P.R. (Ed.), 1998. *Calcareous Nannofossil Biostratigraphy:* Dordrecht, The Netherlands (Kluwer Academic Publishing).

Clemens, S.C., Kuhnt, W., LeVay, L.J., Anand, P., Ando, T., Bartol, M., Bolton, C.T., Ding, X., Gariboldi, K., Giosan, L., Hathorne, E.C., Huang, Y., Jaiswal, P., Kim, S., Kirkpatrick, J.B., Littler, K., Marino, G., Martinez, P., Naik, D., Peketi, A., Phillips, S.C., Robinson, M.M., Romero, O.E., Sagar, N., Taladay, K.B., Taylor, S.N., Thirumalai, K., Uramoto, G., Usui, Y., Wang, J., Yamamoto, M., and Zhou, L., 2016a. Expedition 353 methods. *In* Clemens, S.C., Kuhnt, W., LeVay, L.J., and the Expedition 353 Scientists, *Indian Monsoon Rainfall*. Proceedings of the International Ocean Discovery Program, 353: College Station, TX (International Ocean Discovery Program). **http://dx.doi.org/10.14379/iodp.proc.353.102.2016**

Clemens, S.C., Kuhnt, W., LeVay, L.J., Anand, P., Ando, T., Bartol, M., Bolton, C.T., Ding, X., Gariboldi, K., Giosan, L., Hathorne, E.C., Huang, Y., Jaiswal, P., Kim, S., Kirkpatrick, J.B., Littler, K., Marino, G., Martinez, P., Naik, D., Peketi, A., Phillips, S.C., Robinson, M.M., Romero, O.E., Sagar, N., Taladay, K.B., Taylor, S.N., Thirumalai, K., Uramoto, G., Usui, Y., Wang, J., Yamamoto, M., and Zhou, L., 2016b. Expedition 353 summary. *In* Clemens, S.C., Kuhnt, W., LeVay, L.J., and the Expedition 353 Scientists, *Indian Monsoon Rainfall*. Proceedings of the International Ocean Discovery Program, 353: College Station, TX (International Ocean Discovery Program). **http://dx.doi.org/10.14379/iodp.proc.353.101.2016**

Clemens, S.C., Kuhnt, W., LeVay, L.J., Anand, P., Ando, T., Bartol, M., Bolton, C.T., Ding, X., Gariboldi, K., Giosan, L., Hathorne, E.C., Huang, Y., Jaiswal, P., Kim, S., Kirkpatrick, J.B., Littler, K., Marino, G., Martinez, P., Naik, D., Peketi, A., Phillips, S.C., Robinson, M.M., Romero, O.E., Sagar, N., Taladay, K.B., Taylor, S.N., Thirumalai, K., Uramoto, G., Usui, Y., Wang, J., Yamamoto, M., and Zhou, L., 2016c. Site U1445. *In* Clemens, S.C., Kuhnt, W., LeVay, L.J., and the Expedition 353 Scientists, *Indian Monsoon Rainfall*. Proceedings of the International Ocean Discovery Program, 353: College Station, TX (International Ocean Discovery Program). **http://dx.doi.org/10.14379/iodp.proc.353.105.2016**

Collett, T.S., Riedel, M., Cochran, J., Boswell, R., Presley, J., Kumar, P., Sathe, A.V., Sethi, A., Lall, M., Sibal, V., and the NGHP Expedition 01 Scientists, 2008. *Indian National Gas Hydrate Program (NGHP) Expedition 01, Initial Report:* Noida, India (DGH, Ministry of Petroleum and Natural Gas).

Colin, C., Turpin, L., Bertaux, J., Desprairies, A., and Kissel, C., 1999. Erosional history of the Himalayan and Burman ranges during the last two glacial–interglacial cycles. *Earth and Planetary Science Letters,* 171(4):647–660. **http://dx.doi.org/10.1016/S0012-821X(99)00184-3**

Colin, C., Turpin, L., Blamart, D., Frank, N., Kissel, C., and Duchamp, S., 2006. Evolution of weathering patterns in the Indo-Burman Ranges over the last 280 kyr: effects of sediment provenance on $^{87}Sr/^{86}Sr$ ratios tracer. *Geochemistry, Geophysics, Geosystems,* 7(3):Q03007. **http://dx.doi.org/10.1029/2005GC000962**

Curray, J.R., 1991. Possible greenschist metamorphism at the base of a 22-km sedimentary section, Bay of Bengal. *Geology,* 19(11):1097–1100. **http://dx.doi.org/10.1130/0091-7613(1991)019<1097:PGMATB>2.3.CO;2**

Curray, J.R., 2005. Tectonics and history of the Andaman Sea region. *Journal of Asian Earth Sciences,* 25(1):187–232. **http://dx.doi.org/10.1016/j.jseaes.2004.09.001**

Flores, J.A., Johnson, J.E., Mejía-Molina, A.E., Álverez, M.C., Sierro, F.J., Singh, S.D., Mahanti, S., and Giosan, L., 2014. Sedimentation rates from calcareous nannofossil and planktonic foraminifera biostratigraphy in the Andaman Sea, northern Bay of Bengal, and eastern Arabian Sea. *Marine and Petroleum Geology,* 58(Part A):425–437. **http://dx.doi.org/10.1016/j.marpetgeo.2014.08.011**

Frerichs, W.E., 1971. Planktonic foraminifera in the sediments of the Andaman Sea. *Journal of Foraminiferal Research,* 1(1):1–14. **http://dx.doi.org/10.2113/gsjfr.1.1.1**

Gradstein, F.M., Ogg, J.G., Schmitz, M.D., and Ogg, G.M. (Eds.), 2012. *The Geological Time Scale 2012:* Amsterdam (Elsevier).

Martini, E., 1971. Standard Tertiary and Quaternary calcareous nannoplankton zonation. *In* Farinacci, A. (Ed.), *Proceedings of the Second Planktonic Conference, Roma 1970:* Rome (Edizioni Tecnoscienza), 2:739–785.

Okada, H., and Bukry, D., 1980. Supplementary modification and introduction of code numbers to the low-latitude coccolith biostratigraphic zonation (Bukry, 1973; 1975). *Marine Micropaleontology,* 5:321–325. **http://dx.doi.org/10.1016/0377-8398(80)90016-X**

Singh, S.C., Moeremans, R., McArdle, J., and Johansen, K., 2013. Seismic images of the sliver strike-slip fault and back thrust in the Andaman-Nicobar region. *Journal of Geophysical Research: Solid Earth,* 118(10):5208–5224. **http://dx.doi.org/10.1002/jgrb.50378**

Varkey, M.J., Murty, V.S.N., and Suryanarayana, A., 1996. Physical oceanography of the Bay of Bengal and Andaman Sea. *Oceanography and Marine Biology,* 34:1–70. **http://drs.nio.org/drs/handle/2264/2276**